Title
LOW-ENERGY INTERACTIONS OF K"" MESONS IN HYDROGEN

Authors
Humphrey, William E.
Ross, Ronald R.

Publication Date
1962-01-12

UCRL-10018

University of California

Ernest O. Lawrence Radiation Laboratory

Berkeley, California

DISCLAIMER

UCRL-10018

UNIVERSITY OF CALIFORNIA

Lawrence Radiation Laboratory
Berkeley, California

Contract No. W-7405-eng-48

LOW-ENERGY INTERACTIONS OF K^- MESONS IN HYDROGEN

William E. Humphrey and Ronald R. Ross

January 12, 1962

LOW-ENERGY INTERACTIONS OF K^- MESONS IN HYDROGEN*

William E. Humphrey and Ronald R. Ross

Lawrence Radiation Laboratory
University of California
Berkeley, California

January 12, 1962

ABSTRACT

A study has been made of the K-p interactions in a hydrogen bubble chamber. Cross sections have been determined at 25-Mev/c intervals in the range 75 to 275 Mev/c K^- lab momentum. About 90% of the hyperons were produced by K^--p interactions at rest, and these events were used to calculate at-rest production ratios and hyperon lifetimes.

The observed hyperon decay rates from this experiment yield the following hyperon mean lifetimes:

$$\tau_{\Sigma^-} = (1.58 \pm 0.06) \times 10^{-10} \text{ sec},$$

$$\tau_{\Sigma^+} = (0.765 \pm 0.04) \times 10^{-10} \text{ sec},$$

and

$$\tau_{\Lambda} = (2.69 \pm 0.11) \times 10^{-10} \text{ sec}.$$

The observed branching ratios for Σ^+ and Λ decay are

$$(\Sigma^+ \rightarrow \pi^+ + n) / [(\Sigma^+ \rightarrow \pi^+ + n) + (\Sigma^+ \rightarrow \pi^0 + p)] = 0.490 \pm 0.024,$$

and

$$(\Lambda \rightarrow \pi^- + p) / [(\Lambda \rightarrow \pi^- + p) + (\Lambda \rightarrow \pi^0 + n)] = 0.643 \pm 0.016 .$$

The K^--p interactions occurring at rest yield hyperon production rates in the ratio

$$\Sigma^-: \Sigma^+: \Sigma^0: \Lambda = 0.447: 0.208: 0.281: 0.064.$$

The in-flight K^--p interactions are dominated by the hyperon production process. Analysis of the elastic-scattering angular distribution shows that the nuclear part of the amplitude has a large imaginary part and a real part consistent

with zero. The absorption cross section is nearly geometric for s-wave interactions throughout the observed laboratory momentum range. Angular distributions for all the K^--p interactions are quite consistent with isotropy.

An s-wave zero-effective-range analysis of the K^--p interactions has been carried out. Two sets of parameters were found that give acceptable fits to all the data. The χ^2 test gives probability of 48% for Solution 1, and 8% for Solution 2. The scattering lengths which best fit the data of this experiment are: $A_0 = -0.220 + 2.742\,i$ for the isotopic spin-0 channel, and $A_1 = 0.019 + 0.384\,i$ for the isotopic spin-1 channel.

UCRL-10018

LOW-ENERGY INTERACTIONS OF K^- MESONS IN HYDROGEN

William E. Humphrey and Ronald R. Ross

Lawrence Radiation Laboratory
University of California
Berkeley, California

January 12, 1962

I. INTRODUCTION

This work deals with the interaction of K^- mesons with protons, for K^- momenta less than 275 Mev/c. At such energies, the following interactions can take place:

$$
\begin{aligned}
K^- + p &\rightarrow \Sigma^- + \pi^+ , \\
&\rightarrow \Sigma^0 + \pi^0 , \\
&\rightarrow \Sigma^+ + \pi^- , \\
&\rightarrow \Lambda + \pi^0 , \\
&\rightarrow \Lambda + 2\pi^0 ; \\
\hline
&\rightarrow K^- + p , \\
&\rightarrow K^0 + n , \\
&\rightarrow \Sigma + 2\pi .
\end{aligned}
$$

Those K^- mesons that interact at rest can give rise to the first five interactions. In this experiment, all of the two-body final states have been analyzed to obtain a description of the low-energy interactions in terms of six parameters, by using the formalism of Dalitz and Tuan.[1] In connection with this parameterization, at-rest interactions of K^- mesons were assumed to occur from s-orbitals in accordance with the arguments of Day et al.[2] Other results presented in our paper are angular distributions at production and decay, and hyperon lifetimes.

A large portion of the data included in this work has been reported in the form of preliminary results presented by Luis W. Alvarez at the 1959 Kiev Conference on High Energy Physics.[3] A more detailed discussion of the analysis presented in this paper is available.[4,5]

A summary of data up to 1960 relevent to K^- meson physics has been reported by Freden et al.[6] A detailed analysis has been made of the low-energy elastic K^- meson scattering on free protons in emulsion by Davis et al.[7] Although their results are not included in this analysis, there is excellent agreement between their data and our effective-range solutions. Theoretical discussions pertaining to K^- interactions have been reported by Jackson and Wyld[8] and Dalitz and Tuan.[1]

II. EXPERIMENTAL ARRANGEMENT

The main problem encountered in setting up a K^- beam at the Bevatron is the separation of the K^- mesons from the π^- background. This is difficult in that the π^--to-K^- production ratio is about 1000 to 1 at a secondary beam momentum of 450 Mev/c. Since the π^- mesons live longer than the K^- mesons, this ratio becomes even larger at the detector. In this experiment, the problem was solved by using a coaxial velocity spectrometer developed at Berkeley by Joseph J. Murray.[9] The resulting beam has been described in detail elsewhere,[10] so that only its characteristics at the bubble chamber are given here.

A schematic diagram of the beam is shown in Fig. 1. The momentum before the absorber was 425 Mev/c, and the thickness of the copper absorber was adjusted to give a mean momentum of approximately 180 Mev/c at the center of the chamber. Because of the nonlinear nature of the range-momentum relationship, the momentum distribution at the chamber was very skew.

The flux of K^- mesons was 1 in four pictures. It was limited mainly by the number of background tracks allowed per picture, which was nominally 25.

The background consisted of 85% μ^- and e^-, and 15% π^-. In a total of about 45 000 pictures, we observed approximately 11 000 K^- mesons that either passed through or interacted within the chamber.

III. DATA PROCESSING

A. Scanning

A set of four stereo photographs was taken for each bubble chamber expansion. Approximately 45 000 such stereo sets were examined in accordance with the scanning method described below.

Each picture was scanned in at least two of the four views available. Detection of interactions was accomplished by temporarily masking from view all of the bubble chamber photograph except about a quarter of it, at the end of the chamber through which the beam entered. From the portions of tracks visible at the beam entrance, it was possible to identify the K^- mesons by inspection on the basis of the gap density along the track, and by curvature. Background tracks with few gaps between bubbles (like the gap density of K^- tracks) were of such low momentum that the tracks could be rejected by reason of their high curvature. The number of K candidates in a photograph was recorded, and then the mask was removed to reveal the full picture. Each K candidate was then traced through the picture until the K either interacted, decayed, left the chamber, or was rejected as background. Finally, the result of the track scan was recorded. The track-following method allowed event detection in such a way that the configuration of an interaction had no influence on whether or not an event was discovered by the scanner. Careful second scans show that less than 4% of the K tracks were missed with this scanning technique.

Special emphasis in scanning was placed on the detection of neutral particles from K^--p interactions. When a K^- track terminated in the chamber volume, a search was made of all four views of the chamber to detect any pair of charged particles (these pairs form a "V" which points in the general direction of the interaction) that might represent the decay of a neutral. Since in some cases it is possible for one of the tracks forming the V to be very short, single tracks pointing to the end of the K^- track were also recorded.

The events analyzed in this experiment have been restricted to a central volume of the chamber defined by certain fiducials etched in the top glass of the chamber. The volume was chosen in such a way that events in the region were well illuminated, and particles leaving the interaction vertex were visible over a long enough distance to be measurable. At the scanning stage, events outside of the boundary were recorded, leaving the final selection with respect to the fiducial volume to be made during the computer analysis of each event.

B. Event Processing

Each event identified in the scanning operation has gone through one or more of the following stages:

(a) Sketching—The event is carefully examined and instructions for measuring it are entered onto a card bearing a sketch of the event.

(b) Measuring—A projection microscope digitizes, in cartesian coordinates, the location of 2 to 20 points along particle tracks in the stereo photographs. These coordinate pairs are punched into IBM cards, together with identifying information and measurements of certain fiducials located on the bubble chamber window.

(c) Event computations—A series of IBM 704 programs are used to reconstruct the event in space and determine its kinematic parameters at interaction or decay vertices[4,5] (see Fig. 2).

(d) Remeasurement—Events can fail to be processed through Stage (c) for a large number of reasons, ranging from measuring-machine failure to human errors. It is often necessary to reprocess events several times before obtaining acceptable measurements.

(e) Hand analysis—In the sample of events processed, there were a few events having kinematic or spatial configurations that made them difficult to analyze through the normal channels described above. In these cases, the analysis was done partially by hand, and the results were punched on IBM cards for handling at Stage (f). About 6% of the events were analyzed in this way.

(f) Experiment computations—At this stage all the events processed in the previous stage are examined as a whole, and the parameters of interest in the experiment are determined through a series of IBM 704 programs which use the accumulated information of both machine and hand analysis of individual events. These calculations will be described in more detail in the following section.

IV. ANALYSIS AND RESULTS

A. Path Length for Determination of Cross Sections

The total K^- path length was 1600 m, of which 64.2% was contributed by K mesons passing through the chamber, 29.2% by K mesons that stopped or interacted in flight, and 6.6% by K mesons that decayed. The energy spread of the beam entering the bubble chamber was such that K^- interactions occurred at momenta ranging from about 300 to 0 Mev/c. About 90% of the hyperon interactions occurred at rest. Although the energy spread allows investigation of the entire low-energy region as a whole, there are also complications connected with the wide range of interaction energies. The cross section σ is defined in terms of the relation

$$n = \sigma \ell \left[(\rho N_0)/A \right] , \qquad (1)$$

where $(\rho N_0)/A$ = number of protons per unit volume $(3.5 \times 10^{22}/\text{cm}^3)$,

ℓ = observed K^- track length, and

n = number of interactions observed.

However, since the cross section and the observed path length vary as a function of the momentum interval being considered, two basic tasks must be completed before the cross section can be determined in several momentum intervals.

The first task is the estimation of the path length in the various momentum intervals from 0 to 300 Mev/c. All the K tracks that entered the interaction volume were measured, and the length of path and momentum at an entrance plane were calculated.[4, 5] In the case of the interactions that were fitted, the momentum at the entrance plane was very well known from the kinematic fit of the interaction. However, the rest of the K tracks depended for their momentum measurement

on the observed curvature of the track in the magnetic field of the bubble chamber. These curvature measurements typically had 6 to 10% uncertainties.

The momentum distribution at the entrance plane to the interaction volume has a predominance of tracks in a relatively narrow momentum interval (about 200 to 250 Mev/c). The momentum measurement errors tend to smear out the momentum distribution, which made it necessary to recover the original distribution by unfolding the observed distribution. To do this, the following matrix relationship was used:

$$\underline{L}_o = (\underline{T})\, \underline{L}_t \,, \qquad (2)$$

where $\underline{L}_t$ = vector representing the true number of tracks in each of 12 momentum intervals at the entrance plane,

$\underline{L}_o$ = vector representing the observed number of tracks in each of 12 momentum intervals at the entrance plane,

$\underline{T}_{ji}$ = a matrix element indicating the percentage of events in the $\underline{i}$th true interval that would be observed in the $\underline{j}$th observed interval, on the basis of the typical error for events in the $\underline{i}$th interval.

After solving for $\underline{L}_t$, a range-momentum table was used to establish how much path length was contributed in the various momentum intervals by tracks distributed according to the vector $\underline{L}_t$. This unfolding procedure was applied to events from each of four thicknesses of copper absorber used in this experiment, and these path lengths were accumulated, along with the path length for the interactions, to give the path length per momentum interval displayed in Fig. 3. This path length includes only K track length in the interaction volume not preceded by a visible K-p scatter.

The second task, before the cross sections can be computed, is to estimate the true number of interactions in the various momentum intervals on the basis of the observed momentum distribution. For the hyperon events this procedure is complicated by the fact that the low-energy interactions are plagued by a "background" of stopping interactions. Moreover, the precision with which the momentum of the K is determined varies by as much as a factor of 10, according to the configuration of the individual events. Therefore, a maximum-likelihood estimate was made for the true momentum distribution by using the observed error for each event (see Appendix).

In the choice of momentum-interval widths, we were guided by the desire to measure the cross section as a function of momentum, as accurately as possible. An interval covering all events of the experiment would give an accurate measurement of the average cross section because of the large number of events, but would give no information about the momentum dependence of the cross section. On the other hand, if the intervals were too narrow, the statistical fluctuations of the numbers of events in the individual bins would be large, and uncertainty in the momentum of individual events would cover several bins. The 25-Mev/c width used was a compromise between the two extremes. Errors were propagated to the cross-section estimates from both the matrix-inversion technique and the maximum-likelihood method.

B. Elastic Scattering

A total of 419 elastic scatterings were observed within the fiducial volume. Selection criteria on the minimum angle of scattering and minimum momentum were applied to these events to obviate large and uncertain corrections to the data. The small-angle cutoff was made on the cosine of the center-of-mass (c.m.) angle, in order to have all angular distributions over the same range of $\cos \theta_{c.m.}$. The cutoff was $\cos \theta_{K\,c.m.} = 0.966$, which corresponds to a laboratory-system scattering angle for the K^- of approximately 10 deg over the entire momentum range. For momenta less than 200 Mev/c, the amplitude for Coulomb scattering at this angle is larger than the nuclear amplitude, and the effect of the Coulomb nuclear interference will be clearly indicated by the data. At higher momenta, the Coulomb nuclear interference has less effect on the angular distribution because the maximum interference is at an angle smaller than the cutoff.

Additional selection criteria were applied to the azimuthal angle of the plane of the scattering for events with $\cos \theta_{c.m.}$ between 0.966 and 0.85. Events in this range whose plane of scattering made an angle greater than 30 deg with a vertical plane were accepted. Five events failed this criterion, whereas azimuthal symmetry predicts (from events satisfying the criterion) that 13.5 events should fail. A correction of 3/2 (based on the assumption of azimuthal symmetry) was applied to the events accepted. The events left after application of the small-angle and azimuthal-angle cutoffs are shown in Fig. 4.

A K^- laboratory-system momentum cutoff at 100 Mev/c was imposed for the following two reasons:

(a) The detection efficiency for elastic scatterings is a function of the length of the recoil particles, and therefore decreases rapidly at low momenta.

The residual range for K^- mesons of 100 Mev/c is a little over 1.5 cm in liquid hydrogen. When they scatter at 180 deg from a proton they are left with a residual range of 0.2 mm, which is not enough to make one bubble (one bubble $\approx$ 0.25 mm); however, the proton has a range of 0.7 cm and is easily detected. At 75 Mev/c the residual range of the K^- is down to 0.5 cm, and the corresponding 180-deg scattering produces a proton with a range of about 3 mm. In scatterings at angles less than 180 deg at these momenta, both proton and K^- tracks are very short. Because of the short recoil tracks, we must take into account that a K^- meson coming to rest in liquid hydrogen makes charged hyperons more than half the time. Pictures of this type of event have two densely ionizing tracks and one light one, all meeting at a point. The charged hyperon and π meson are collinear, but have random orientation with respect to the K^- direction. There is, therefore, some probability that the elastic scatterings at low momenta preceding this type of event will be obscured.

(b) The other effect that requires a 100-Mev/c cutoff is the distortion of track images caused by nonuniform density of liquid hydrogen in the light path from track to film. We observed displacements of the images of tracks by as much as a track width over lengths of track from 1 mm to 0.5 cm. The effect could be compensated for if it were in the middle of a long track, but those cases in which the distortion was in the last 0.5 cm of the incident K^- were very difficult to interpret. These factors, giving rise to large uncertainties in scanning biases at low momenta, coupled with the fact that only 13 events are observed between 50 and 100 Mev/c, made it necessary to apply this cutoff at 100 Mev/c.

Two sources of systematic error in the number of events observed at small angles were considered. The first concerns an enhancement of the number of large-angle events observed owing to uncertainty in the value of the measured angle of scattering. Since individual measurements of the angle of scattering are, to first approximation, distributed symmetrically about the true angle of scattering, and since uncertainty of measurement does not vary rapidly with angle, the probability of observing a 9-deg scattering at 11 deg is the same as the probability of observing an 11-deg scattering at 9 deg. However, the $[1/\sin^4(\theta/2)]$ dependence of the Coulomb cross section gives more events truly at 9 than at 11 deg, and so the number observed at 11 deg is systematically increased. Corrections for this effect were calculated on the assumption that the angular distribution is given by the Coulomb cross section out to angles where the Coulomb cross section is equal to the nuclear cross section. No corrections were applied beyond this angle.

The second source of systematic error considered was that due to Molière or plural scattering. For the angles considered, Molière scattering can be represented as an effective increase in the Coulomb scattering cross section. Bethe has derived a formula for the asymptotic ratio of Coulomb to actual scattering,[11] and calculations of this ratio for path length of 0.5 cm of liquid hydrogen showed the effect to be small. The largest correction was 2%. No corrections were necessary in the region -1.0 to 0.85 in $\cos\theta_{c.m.}$.

To determine cross sections as a function of momentum and angle, the events of Fig. 4 were divided into four intervals in $\cos\theta_{c.m.}$, and ten intervals in momentum. Because of the isotropic nature of the distribution in the region where Coulomb scattering is small ($\cos\theta_{c.m.} < 0.85$), the data in this region were all

lumped into one cos θ interval. The three intervals in cos $\theta_{c.m.}$, 0.85 to 0.90, 0.90 to 0.095, and 0.95 to 0.966, were chosen to give a maximum amount of information about the Coulomb nuclear interference. The events in each angular region were analyzed separately as a function of momentum, as described in Sec. IVA. The final estimates of the number of events per momentum interval for K^- lab momentum greater than 100 Mev/c were converted to cross sections by the use of Eq. (1) and the path length shown in Fig. 3.

The total elastic-scattering cross sections for values of cos $\theta_{c.m.}$ between -1.0 and 0.966 are presented in Fig. 5 and Table I. These values are the sums of cross sections observed in the four angular intervals, and therefore contain Coulomb as well as nuclear scattering. The uncertainties shown in Fig. 5 are the square roots of the diagonal terms of the variance-covariance matrix of Table I. The solid curve is the cross section calculated by using the parameters of Solution 1 (Table XIII).

It was considered desirable to determine the modulus and phase of the nuclear part of the elastic-scattering amplitude, independent of the s-wave zero-effective-range theory. To get a statistically significant estimate of the scattering amplitude, we determined two average differential-scattering cross sections by averaging the cross sections for each angular region over groups of three momentum intervals. The average differential-scattering cross sections for the intervals 100 to 175 Mev/c, and 175 to 250 Mev/c K^- lab momentum are shown in Fig. 6. In Sec. V-D, we show how the nuclear part of the scattering amplitude has been estimated from these cross sections.

C. Charge-Exchange Scattering

A $\bar{K}^0$ production event is detectable when the $\bar{K}^0$ decays via one of its charged modes, or when it interacts in the hydrogen in such a way as to produce charged particles. Of the 29 $\bar{K}^0$ events observed, 25 were normal K_1^0 decays,

$$K_1^0 \rightarrow \pi^+ + \pi^- ,$$

and formed the sample used for calculation of the cross section as a function of momentum. In addition, there were two inelastic scatterings giving rise to hyperons. The first scattering was identified as

$$\bar{K}^0 + p \rightarrow \Sigma^+ + \pi^0 ,$$

followed by $\Sigma^+ \rightarrow p + \pi^0$; the second as

$$\bar{K}^0 + p \rightarrow \Lambda + \pi^+ ,$$

followed by $\Lambda \rightarrow p + \pi^-$.

Two other $\bar{K}^0$ events were examples of the K_2^0 decay into three-body final states. The observation of two K_2^0 decays is consistent with the published lifetime of $6.1(+1.6/-1.1)\times10^{-8}$ sec.[12]

Care was taken to distinguish between the $\bar{K}^0$ decays and the Λ-hyperon decays. Ambiguities in the identification of these V events arise only if the proton of the Λ decay cannot be distinguished from the π^+ of the K_1^0 decay. In a total of about 1000 V's, only five cases were ambiguous at the scanning stage, and a kinematical analysis of these events for both interpretations yielded unambiguous identification for all five. Three were Λ events and two were K_1^0.

We used only K_1^0 of length > 1 mm, to avoid ambiguity between events with short $\bar{K}^0$ and short Σ tracks. The similarity in momenta of the π's in the interactions

$$K^- + p \rightarrow \Sigma^{\pm} + \pi^{\mp} \quad \Sigma^{\pm} \rightarrow \pi^{\pm} + n,$$

and

$$K^- + p \rightarrow \bar{K}^0 + n \quad \bar{K}^0 \rightarrow \pi^+ + \pi^-,$$

makes kinematical separation impossible for many spatial configurations if the Σ or $\bar{K}^0$ track is too short to be seen. It was often possible to fit both hypotheses.

Application of the 1-mm cutoff eliminated one of the 25 detected events. For each of the remaining K_1^0's we calculated the probability of the $\bar{K}^0$ length being less than 1 mm, and the probability of escaping the volume. In this way the observed K_1^0's served as an estimate of the spatial and momentum distribution of the complete sample. The calculations indicated that 17.8% (5.25 events) should be less than 1 mm long, and that 0.9% (1/3 of an event) should escape the volume. The lifetime used for these corrections was 0.95×10^{-10} sec.[12] Corrections were also made for the fact that only one-third of the $\bar{K}^0$'s produced decay via the charged K_1^0 mode.

In Fig. 7 we show a scatter diagram of the 25 $\bar{K}^0$ events. The χ^2 for the hypothesis of an isotropic angular distribution is 3.8 for three degrees of freedom. Cross sections calculated from the maximum-likelihood estimates are presented in Fig. 8 and Table II. The uncertainties in the cross sections shown in Fig. 8 are the square roots of the diagonal terms in the variance-covariance matrix of Table II. The solid curve in Fig. 8 is the cross section calculated by using the parameters of Solution 1 (Table XIII).

D. Hyperon Production

Several selection criteria were applied to the hyperon events. A 0.1-cm cutoff on the hyperon length and a 20-deg K-hyperon-angle cutoff served two purposes: First, it made analysis of the poorly determined and hard-to-measure events unnecessary; and secondly, it eliminated from consideration nearly all the events in the ambiguous classes. In order to compensate for the events culled from the sample, the probability for observing each event was calculated on the basis of the selection criteria, the momentum of the hyperon, and the hyperon lifetime. For the Σ particles the acceptance probability for each event accepted was given by

$$A_{\Sigma} = \exp\left[-t_c/\tau\right] \quad \frac{\cos\theta_f - \cos\theta_b}{2} \ , \tag{3}$$

where

t_c = time required for the Σ to travel the cutoff distance of 0.1 cm,

τ = lifetime of Σ,

θ_f = forward cutoff angle in the c.m. system, and

θ_b = backward cutoff angle in the c.m. system.

Corrections for culled Λ hyperons were carried out in much the same way as for the Σ analysis, except that an escape correction was included for each event, since only Λ decays within the interaction volume were considered. As a consequence, the acceptance probability for each Λ event was computed as

$$A_{\Lambda} = \exp\left[-t_c/\tau\right] - \exp\left[t_e/\tau\right] \ , \tag{4}$$

where

t_c = time required for the Λ to travel the cutoff distance of 0.1 cm,

t_e = time required to escape through the nearest boundary plane of the interaction volume, and

τ = lifetime of Λ.

Additional corrections were found to be necessary in the hyperon analysis. Careful examination of the ambiguous Σ classes revealed that there were some Σ events that were actually longer than 0.1 cm (and should have been included in the analysis), but the Σ was hard to identify because the π decayed almost collinearly with respect to the Σ. This effect was taken into account by calculating the estimated number of Σ particles having the above properties. The number of events was calculated to be 20 Σ^+ and 30 Σ^- events, which should have been included in the analyzed sample. The cross sections were corrected for these events by an overall scaling factor. These additional events were predominantly short (i.e., just greater than 0.1 cm); hence, their principal effect was to modify the lifetime estimates slightly, necessitating a lifetime correction. A similar calculation was made for the ambiguous Λ class, and the additional number of Λ events which should have been analyzed was estimated to be ten. The Λ cross section was corrected for these events. The estimates for the hyperon production cross sections are shown in Figs. 9 and 10 and summarized in Tables III, IV, and V. For each charged Σ event giving an in-flight fit, the laboratory momentum and c.m. cosine have been plotted on a scatter diagram (Figs. 11 and 12).

The most reliable value of the $\Lambda/(\Sigma^0 + \Lambda)$ ratio is the one obtained for Λ production by K interactions at rest, where the separation between direct and indirect Λ's can almost be done by inspection (see Fig. 13). Four of the events, with an energy near 35 Mev, are interpreted as $K^- + p \rightarrow \gamma + \Lambda$, which implies a branching ratio for this process of about 0.8% of the total Λ production. There is a cluster of events at 40 Mev, two of which have energies that are well-determined and within errors of each other. These events are interpreted as in-flight K interactions. The $\Lambda/(\Sigma^0 + \Lambda)$ separation was done by the maximum-likelihood method

for K interactions, both at-rest and in-flight (Fig. 14). Seven events with energies in excess of three standard deviations from either the Λ or the Σ^0 spectrum were not included in the likelihood calculations.

The number of Σ^+ and Σ^- hyperons produced at rest is readily available from Table VI. The number of Σ^0 and Λ hyperons can be calculated by using Table VI and the $\Lambda/(\Sigma^0 + \Lambda)$ ratio of 0.186±0.017. The numbers obtained in this way yield the ratio $\Sigma^-:\Sigma^+:\Sigma^0:\ \Lambda = 1553:722:977:223$. The reaction amplitudes can then be calculated and resolved into I-spin-0 and I-spin-1 channels for Σ production. The results can be expressed in terms of the ratio of I-spin-0 and I-spin-1 amplitudes for the Σ mode and their relative phase, plus the ratio of the Λ I-spin-1 amplitude to the Σ I-spin-1 amplitude. These quantities (after phase-space corrections) have been determined to be:

$$\left| \frac{A_{\Sigma_1}}{A_{\Sigma_0}} \right| = 0.37 \pm 0.06,$$

$$\cos \phi_{\Sigma_0 \Sigma_1} = 0.51^{+0.14}_{-0.10},$$

and

$$\left| \frac{A_{\Sigma_1}}{A_{\Lambda_1}} \right| = 1.57 \pm 0.23.$$

E. Hyperon Decay

1. Angular Distributions for Hyperon Decay

The cosine of the angle between the Σ and its decay pion (in the rest frame of the Σ) has been calculated for the unambiguous Σ decays. Ambiguous events between Σ^+ and Σ^- contribute a correction of about 30 events for Σ^-, and 20 events for Σ^+, in the region $|\cos\theta_{\Sigma\pi}| > 0.8$. Not included in these figures are 26 Σ^+ events and 66 Σ^- events that were hand analyzed only at the production vertex. No particular bias is expected from these events. The cosine of the angle between the Λ and its decay pion (in the rest frame of the Λ) was calculated for direct Λ production and also for Λ's from Σ^0 decay. The events were selected to include only events from K interactions having measured momenta less than 75 Mev/c, because such events represent the at-rest K interactions for which the kinematics are well enough determined to give a reliable separation between direct and indirect Λ production. Fourteen events, hand analyzed only at the production vertex, have not been included. No appreciable bias is expected from these events. There is less than 5% contamination by events which are not from K^--p at-rest interactions.

The energy distribution for Λ hyperons produced by at-rest K^--p interactions is given in Fig. 13. The $\Sigma^0 \rightarrow \gamma + \Lambda$ energy spectrum can be interpreted as a cosine distribution for the Λ with respect to the Σ^0 direction in the Σ^0 c.m. system, as is seen from the relation

$$E_{\Lambda K^- p} = -\eta P_{\Lambda\Sigma}\cos\theta + \gamma E_{\Lambda\Sigma} \qquad (5)$$

where

$P_{\Lambda\Sigma}$ = Λ momentum in the Σ^0 c.m. system (a constant),

$E_{\Lambda\Sigma}$ = Λ energy in the Σ^0 c.m. system (a constant),

$\gamma^2 = 1 + \eta^2$, and

$\eta = \frac{P_\Sigma}{M_\Sigma}$ in the K-p center-of-mass (a constant).

The various cosine distributions mentioned above have been fit to a quadratic, by using the least-squares method (Table VII).

2. Hyperon Lifetimes

The lifetime of the Σ's was determined by using the maximum-likelihood method. All events with Σ < 0.1 cm long, or a Σ-K angle < 20 deg, were not included in the analysis. Only Σ's produced by K^- interactions at rest were used for lifetime estimates, because the Σ momentum is well-determined for these events. The Σ's that decayed in the last 0.2 cm of their range were considered to have lived a time exceeding that required to reach the 0.2-cm cutoff (this cutoff is to simplify the problem of separating Σ^- events that decay with the Σ^- at rest).

The probability for observing a given event in each of the two classes is then

$$\text{(a)} \quad \frac{dP_i}{dt_i} = \lambda \frac{\exp\left[-\lambda t_i\right]}{\exp\left[-\lambda t_c\right]} \quad \text{for } t_c < t_i < t_m, \text{ or}$$

$$\text{(b)} \quad P_i = \frac{\exp\left[-\lambda t_m\right]}{\exp\left[-\lambda t_c\right]} \quad \text{for } t_i > t_m, \qquad (6)$$

where

t_i = observed time for the ith event,

t_c = time to travel 0.1 cm from production point,

t_m = time to travel within 0.2 cm of end of range, and

λ^{-1} = mean life.

This probability is normalized to give unit probability for observing Σ's with a length exceeding 0.1 cm. This corresponds to the assertion that once the length is measured to exceed 0.1 cm, the integral of the probability for this sample must integrate to unity beyond 0.1 cm.

As a consistency check, two different likelihood functions, L_1 and L_2, were considered. First we form the product of the likelihood function for each event and take the log, to give

$$\ln L_1 = \ln \prod_{i=1}^{N} P_i = \sum_{i=1}^{N} \ln P_i = \sum_{i=1}^{N_1} (\ln\lambda - \lambda t_i + \lambda t_c) + \sum_{k=1}^{N_2} (\lambda t_c - \lambda t_m) \quad , \tag{7}$$

and the maximum of this function is located at

$$1/\lambda = 1/N_1 \left[\sum_{i=1}^{N_1} (t_i - t_c) + \sum_{k=1}^{N_2} (t_m - t_c) \right] \quad , \tag{8}$$

with $\overline{\delta\lambda^2} = - (d^2 \ln L_1/d\lambda^2)^{-1} = (N_1/\lambda^2)^{-1}$,

where

λ = decay rate,

N_1 = number of events with $t_c < t_i < t_m$, and

N_2 = number of events with $t_i > t_m$.

Secondly, as a consistency check, the lifetime was determined, neglecting the events with $t_i > t_m$. In this case, one has

$$P_i = \frac{\lambda \exp(-\lambda t_i)}{\exp(-\lambda t_c) - \exp(-\lambda t_m)} \quad , \; t_c < t_i < t_m ; \tag{9}$$

$$\ln L_2 = \sum_{i=1}^{N_1} \left\{ \ln\lambda - \lambda t_i - \left[\ln \left[\exp(-\lambda t_c) - \exp(-\lambda t_m) \right] \right] \right\} \quad ; \tag{10}$$

and one has L_2 a maximum at

$$1/\lambda = 1/N_1 \sum_{i=1}^{N_1} \left\{ t_i + \frac{t_m \left[\exp(-\lambda t_m)\right] - t_c \left[\exp(-\lambda t_c)\right]}{\exp(-\lambda t_c) - \exp(-\lambda t_m)} \right\} , \tag{11}$$

and

$$\overline{\delta\lambda^2} = \left\{ N_1/\lambda^2 - \sum_{i=1}^{N_1} \frac{(t_m - t_c)^2 \exp\left[-\lambda(T_m + T_c)\right]}{\left[\exp\left[(-\lambda t_c)\right] - \exp\left[(-\lambda t_m)\right]\right]^2} \right\}^{-1} . \tag{12}$$

We found λ (using the L_2 formulation) by iteration, because the relation for λ is a transcendental one. In the case of Λ decay, where the Λ may decay outside the chamber, the second formulation (L_2) is the only applicable one. For the Λ's, t_c was defined as for the Σ's but t_m was taken as the time for the Λ to reach the nearest boundary of the interaction volume.

As mentioned in Sec. IV-D-3, a correction was applied to the Σ lifetimes to account for events in the ambiguous catagories which really should have been included in the lifetime calculation, because their length exceeded 0.1 cm. The number of such events was estimated as 20 for Σ^+, and 30 for Σ^-. The model used to calculate the number of events was also used to calculate the amount of time they contribute to the lifetime calculation, and these numbers were inserted in the previous equations to obtain the corrected lifetimes. A small correction was applied to the Σ^- lifetime to account for the Σ^--p interactions in flight. The corrections decreased both the Σ^+ and Σ^- lifetime by 0.01×10^{-10} sec. The results of the lifetime calculations are shown in Table VIII.

The branching ratio between neutral and charged Λ decay was determined by counting the number of K tracks that stopped in the fiducial volume of the chamber with no visible hyperon decay. This number was corrected for neutral $\bar{K}^0$ decays and Λ decays outside of the chamber (a correction of 54 events). The ratio obtained was

$$\frac{\Lambda \text{ charged}}{\Lambda \text{ total}} = \frac{903}{1405} = 0.64 \pm 0.01 .$$

The branching ratio between neutron and proton decay modes of Σ^+ hyperons was found to be

$$\frac{\Sigma^+ \text{ neutron}}{\Sigma^+ \text{ total}} = \frac{308}{628} = 0.49 \pm 0.02.$$

There were 17 events ambiguous between proton and neutron decay modes; these events were divided equally between the two modes for the purpose of calculating the branching ratio. The error in the branching ratio includes a contribution for these ambiguous events.

These branching ratios are in excellent agreement with the $\Delta I = 1/2$ rule.[13]

V. DISCUSSION OF RESULTS

A. Decay Rates and the $\Delta I=1/2$ Rule

The $\Delta I=1/2$ rule makes a definite prediction for the ratio of the decay matrix elements for $\Lambda \to \pi^0 + n$ and $\pi^- + p$ decay.[13] The prediction is

$$\frac{s_-^2 + p_-^2}{(s_-^2 + p_-^2) + (s_0^2 + p_0^2)} = \frac{2}{3}, \tag{13}$$

where s_- and p_- are s- and p-wave amplitudes for the $\pi^- + p$ decay mode, and s_0 and p_0 are s- and p-wave amplitudes for the $\pi^0 + n$ decay mode. The experimental branching ratio from this experiment is

$$\frac{(\pi^- + p)}{(\pi^0 + n) + (\pi^- + p)} = 0.643 \pm 0.016,$$

which, after taking account of phase space for the two decay modes, yields the value

$$\frac{s_-^2 + p_-^2}{(s_-^2 + p_-^2) + (s_0^2 + p_0^2)} = 0.650 \pm 0.016 .$$

Another interesting (but less constraining) prediction following from the $\Delta I=1/2$ rule concerns the relative size of the amplitudes for the three decay modes of charged Σ hyperons. If the s and p amplitudes for a single decay mode are represented as a two-dimensional vector, then the $\Delta I = 1/2$ rule predicts the following vector relationship:[13]

$$\sqrt{2}\,\underline{A}_0 + \underline{A}_+ = \underline{A}_- , \tag{14}$$

where

$\underline{A}_0$ corresponds to $\Sigma^+ \to \pi^0 + p$,

$\underline{A}_+$ corresponds to $\Sigma^+ \rightarrow \pi^+ + n$, and

$\underline{A}_-$ corresponds to $\Sigma^- \rightarrow \pi^- + n$.

The decay rates for the three decay modes have been determined in this experiment to be:

$$R_0 = (0.666 \pm 0.047) \times 10^{10}/\text{sec},$$
$$R_+ = (0.641 \pm 0.046) \times 10^{10}/\text{sec, and}$$
$$R_- = (0.634 \pm 0.025) \times 10^{10}/\text{sec}.$$

Therefore, the amplitudes (including the phase space correction) have relative sizes

$$|\underline{A}_0| = 0.544 \pm 0.019,$$
$$|\underline{A}_+| = 0.540 \pm 0.019, \text{ and}$$
$$|\underline{A}_-| = 0.527 \pm 0.010.$$

The resulting vector triangle has an angle between $\underline{A}_-$ and $\underline{A}_+$ of 92.4 ± 4.8 deg. Measurements of the decay asymmetries for Σ^+ decay reveal that the vector $\underline{A}_0$ must have appreciable components of both s- and p-wave amplitudes, while $\underline{A}_+$ must be an almost pure s or p wave.[14] Other experimental evidence suggests that $\underline{A}_-$ is also almost pure s or p wave.[15] Hence the vector triangle has the remarkable property that it appears to be nearly a right triangle, with its legs about 1 deg from the s and p axes. Theoretical significance has been attached to this striking alignment of the triangle in a paper by A. Pais,[16] in which the suggestion is made that the weak as well as the strong interactions might be coupled through a doublet approximation model of the elementary particles.

The experimental results are certainly very consistent with the predictions of the $\Delta I = 1/2$ rule; however, only the magnitudes of the decay amplitudes are observable in this experiment and not the phases. It has been pointed out that

appropriate mixtures of $\Delta I=1/2$ and $\Delta I=3/2$ can give rise to the same physical consequences as the $\Delta I=1/2$ rule, but with certain phases shifted by 180 deg.[17]

B. Hyperon Spins

The spin of the hyperons has been determined by previous experiments;[18, 19, 20] however, further evidence is available from this experiment, subject to two assumptions. First, it is assumed that the K meson has spin zero.[19] Secondly, K interactions that occur at rest are assumed to take place from s orbits in accordance with the calculations of Day et al.[2] If we make these assumptions, it is clear that the angular momentum of the initial state is $J = 1/2$. Therefore, the maximum angular momentum component along the direction of the Σ cannot exceed 1/2, by conservation of the component of J projected along the Σ. This means that if the Σ hyperon spin is greater than 1/2, certain spin states with angular momentum components in excess of 1/2 along the Σ direction are forbidden. As a result, only spin 1/2 can give an isotropic distribution.[20] Spin 3/2 gives a distribution of the form $1 + 3\cos^2\theta$.

The Σ^+ and Σ^- decay distributions for K^- interactions at rest have been fitted to distributions of the form $N = a_1 + a_2\cos\theta + a_3\cos^2\theta$. The results shown in Table VII provide strong evidence that both Σ^- and Σ^+ are spin 1/2 particles. The same argument applies to the directly produced Λ hyperons; the result recorded in Table VII strongly indicates isotropy, hence spin 1/2 for the Λ.

The Σ^0 spin can be established with certainty under the assumption of odd $\Sigma^0 - \Lambda$ parity, in which case, it is possible to show that the $\Sigma^0 - \Lambda$ distribution is isotropic for spin 1/2, and is $(1 + 0.6\cos^2\theta)$ for spin 3/2.[21] Again, isotropy is highly favored, as can be seen from Table VII.

C. Determination of s-Wave Zero-Effective-Range Parameters

The data presented in Sec. IV have been combined to determine parameters for an s-wave zero-effective-range theory of the K^--p interaction. In 1958 Jackson et al. suggested the use of a zero-effective-range theory for parameterizing the K^--p interactions.[22] Since that time, many refinements have been made in the theory to adapt it to the K^--p system.[1,8,23] For instance, the K(reaction)-matrix formalism, has been introduced in order to handle charge-dependent effects related to the $\bar{K}^0$-n — K^--p mass difference without sacrificing the charge-independent nature of the nuclear matrix elements. Coulomb effects (important at low momenta) have been included. The results of Dalitz and Tuan have been used in the analysis.[1] In their notation, the equations for the cross sections given in this theory are

$$\frac{d\sigma_{el}}{d\Omega} = \left| \frac{\csc^2(\theta/2)}{2Bk^2} \exp\left[\frac{2i}{kB} \ln \sin(\theta/2)\right] + \frac{C^2/2\left[A_0(1-ik_0A_1)+A_1(1-ik_0A_0)\right]}{D} \right|^2 \quad (15)$$

$$\sigma_{ch.ex.} = \frac{\pi k_0 C^2}{k} \left| \frac{A_0 - A_1}{D} \right|^2, \quad (16)$$

$$\sigma_0 = \frac{4\pi b_0 C^2}{k} \left| \frac{1-ik_0A_1}{D} \right|^2, \quad (17)$$

and

$$\sigma_1 = \frac{4\pi b_1 C^2}{k} \left| \frac{1-ik_0A_0}{D} \right|^2, \quad (18)$$

where

$$D = 1 - i\left[k_0 + C^2k(1-i\lambda)\right]\left(\frac{A_0+A_1}{2}\right) - k_0\left[C^2k(1-i\lambda)\right]A_0A_1.$$

$A_0 = a_0 + ib_0$ = the complex scattering lengths for the isotopic-spin 0 and 1 channels, respectively.
$A_1 = a_1 + ib_1$

k_0 = the wave number (center-of-mass system) of the $\bar{K}^0 N$ channel (taken as $i\,|k_0|$ below $\bar{K}^0 N$ threshold),

k = the center-of-mass wave number of the K^--p channel,

C^2 = the Coulomb penetration factor = $\frac{2\pi}{kB}\left[1-\exp\left(-2\pi/kB\right)\right]^{-1}$

B = the Bohr radius of the K^--p system,

λ = a function of k given by the authors'[1] Eq. (4.12), and

σ_0 and σ_1 = the absorption cross sections in the I=0, I=1 channels, respectively.

Besides the four real parameters contained in A_0 and A_1, two more parameters are necessary to express the observed hyperon cross sections. We chose these parameters as the ratio γ of $\Sigma^- \pi^+$ to $\Sigma^+ \pi^-$ production at rest, and the ratio ϵ of the $\Lambda\pi^0$ production rate to the total hyperon production rate in the isotopic spin-1 channel at rest. In our analysis we have assumed the following conditions to hold for the parameters of the theory:

(a) The scattering lengths A_0 and A_1 are independent of momentum,

(b) The parameter ϵ is independent of momentum, and

(c) The momentum dependence of the difference in phase angle, $\phi = \phi_0 - \phi_1$, between the matrix elements for $\Sigma\pi$ production in I=1 and I=0, is given by

$$\phi = \phi_{th} + \arg \frac{1-ik_0A_1}{1-ik_0A_0}\,, \qquad (19)$$

where ϕ_{th} = the value of the phase angle at the $\bar{K}^0$-n threshold (89-Mev/c incident K^- lab momentum). Condition (c) is used to relate γ

to the value of ϕ_{th}, and therefore γ is the parameter that determines the phase ϕ.

The assumption that the capture of K^- on protons at rest takes place with the K^--p system in a relative s state[2] allows the use of the at-rest ratios of the hyperon production rates that are so important in determining the values of the parameters. In terms of $\phi, \epsilon, \sigma_0(A_0, A_1)$, and $\sigma_1(A_0, A_1)$, the hyperon cross sections are given by

$$\sigma(K^- + p \to \Sigma^- + \pi^+) = \frac{1}{6}\sigma_0 + \frac{1}{4}(1-\epsilon)\sigma_1 + \left[\frac{\sigma_0\sigma_1(1-\epsilon)}{6}\right]^{\frac{1}{2}} \cos\phi , \tag{20}$$

$$\sigma(K^- + p \to \Sigma^+ + \pi^-) = \frac{1}{6}\sigma_0 + \frac{1}{4}(1-\epsilon)\sigma_1 - \left[\frac{\sigma_0\sigma_1(1-\epsilon)}{6}\right]^{\frac{1}{2}} \cos\phi , \tag{21}$$

$$\sigma(K^- + p \to \Sigma^0 + \pi^0) = \frac{1}{6}\sigma_0 , \tag{22}$$

and

$$\sigma(K^- + p \to \Lambda + \pi^0) = \frac{1}{2}\sigma_1\epsilon , \tag{23}$$

where σ_1 and σ_0 are given by Eqs. (17) and (18). In addition, the at-rest ratios are

$$\left.\frac{\Gamma(K^- + p \to \Lambda + \pi^0)}{\Gamma(K^- + p \to \Lambda + \pi^0) + \Gamma(K^- + p \to \Sigma^0 + \pi^0)}\right|_{\text{at rest}} = \frac{\epsilon b_1 \left|1 + \kappa A_0\right|^2}{\epsilon b_1 \left|1 + \kappa A_0\right|^2 + \frac{1}{3} b_0 \left|1 + \kappa A_1\right|^2} , \tag{24}$$

$$\left.\frac{\Gamma(K^- + p \to \Sigma^- + \pi^+)}{\Gamma(K^- + p \to \Sigma^+ + \pi^-}\right|_{\text{at rest}} =$$

$$\frac{\left[\frac{b_0}{6}\left|1 + \kappa A_1\right|^2\right] + \left[\frac{(1-\epsilon)b_1}{4}\left|1 + \kappa A_0\right|^2\right] + \left|1 + \kappa A_0\right| \cdot \left|1 + \kappa A_1\right| \left[\frac{(1-\epsilon)}{6}\right]^{1/2} \cos\phi}{\left[\frac{b_0}{6}\left|1 + \kappa A_1\right|^2\right] + \left[\frac{(1-\epsilon)b_1}{4}\left|1 + \kappa A_0\right|^2\right] - \left|1 + \kappa A_0\right| \cdot \left|1 + \kappa A_1\right| \left[\frac{(1-\epsilon)}{6}\right]^{1/2} \cos\phi} , \tag{25}$$

and

$$\left.\frac{\Gamma(K^- + p \to \Sigma^- + \pi^+) + \Gamma(K^- + p \to \Sigma^+ + \pi^-)}{\Gamma(K^- + p \to \Sigma^0 + \pi^0) + \Gamma(K^- + p \to \Lambda + \pi^0)}\right| = \frac{\frac{b_0}{6}\left|1+\kappa A_1\right|^2 + \left[\frac{(1-\epsilon)b_1}{2}\left|1+\kappa A_0\right|^2\right]}{\frac{b_0}{6}\left|1+\kappa A_1\right|^2 + \frac{\epsilon b_1}{2}\left|1+\kappa A_0\right|^2}, \quad (26)$$

at rest.

where κ is the absolute value of the wave number in the $\bar{K}^0$-n channel for zero K^--p relative momentum [i.e., $\kappa = |k_0 (P_{K^-} = 0)|$].

Many pieces of experimental data are available for the determination of the parameters. These data are presented by $\sigma_{aj}{}^m$, where m stands for "measured." The symbol a takes on the integer values from 1 to 12, depending on the physical process for which a measurement has been made, and j varies with the lab momentum of the K^- for which the measurement was made. A zero value for j means a measurement at rest; j = 1 corresponds to the momentum interval $0 \leq P_K \text{lab} \leq 25$ Mev/c, and so on for 25-Mev/c intervals. In Table IX we indicate which measurements have contributed to the determination of the parameters.

A value corresponding to each measurement was calculated from the theory by assuming values for the parameters. We then calculated a χ^2 for the experiment, from the equation

$$\chi^2(A_0, A_1, \gamma, \epsilon) = \sum_{a=1}^{12} \sum_{j=a_a}^{b_a} \sum_{k=a_a}^{b_a} (\sigma_{aj} - \sigma_{aj}{}^m)(E^a)_{jk}^{-1}(\sigma_{ak} - \sigma_{ak}{}^m), \quad (27)$$

where E^a is the variance-covariance matrix for measurements in the class a.

The minimum in the χ^2 function was found by numerically evaluating the first and second derivatives of the function with respect to each variable, and then moving the one variable which predicted the greatest reduction in the χ^2. The starting values chosen for the parameters were the estimates recently calculated by Dalitz for the a^+, a^-, b^+, and b^- solutions.[24] The a^+ and b^- starting values led to the same minimum, and the a^- and b^+ starting values led to a second lower minimum. The starting values and the solutions derived from them are presented in Table X.

Under the assumption that χ^2 is a quadratic function of the parameters in the region of the minimum, we can write

$$\chi^2(\underline{\beta}) = (\underline{\beta}-\underline{\beta}^*) \cdot \underline{D} \cdot (\underline{\beta}-\underline{\beta}^*) + \chi^2(\underline{\beta}^*) . \qquad (28)$$

The elements of the matrix $\underline{D}$ were found by exploring the χ^2 space in the neighborhood of the minimum. We have taken two times the inverse of $\underline{D}$ as an estimate of the variance-covariance matrix ($\underline{V}$) for the parameters. The values of the parameters giving the lowest χ^2, the matrix $\underline{D}$, and the variance matrix for these parameters, are given in Tables XI and XII. The matrix $\underline{D}$ allows predictions of the change in χ^2 that are good to about 30% for variations of parameters within a range of 1 or 2 standard deviations of the values at the minimum. The χ^2 space appears to be skew for several of the parameters.

Tables XIII and XIV list the properties of the K^--p system predicted by the two solutions. The predictions for Solution 1 have been compared with the experimental data in Figs. 5, 8, 9, 10, and 14. The contribution to the total χ^2 from each piece of data is displayed in Table XV.

D. Coulomb Nuclear Interference

The s-wave zero-effective-range analysis above does contain information on the Coulomb nuclear interference, but the inclusion of all other information partially obscures its part in the final solution. For this reason it was considered desirable to analyze the Coulomb nuclear interference separately, independent of any assumptions on the momentum dependence or isotopic-spin dependence of the cross section. To this end, we write the differential-scattering cross section for K^--p elastic scattering in the form

$$\frac{d\sigma_{el}}{d\Omega} = \left| \frac{\csc^2(\theta/2)}{2Bk^2} \exp\left[i \frac{2}{kB} \ln \sin\left(\frac{\theta}{2}\right)\right] + C^2 R \exp\ (ia) \right|^2 . \tag{29}$$

The first term on the right is the Coulomb part of the scattering amplitude, k is the center-of-mass wave number, and B is the Bohr radius of the K^--p system. The second term represents the s-wave nuclear amplitude (modified by C^2, the real s-wave Coulomb penetration factor); hence, R cos a and R sin a are the real and imaginary parts, respectively, of the nuclear amplitude. The Coulomb amplitude is dominant at small angles, but decreases rapidly with increasing angle. At some angle θ_c the Coulomb amplitude will be equal in magnitude to the nuclear amplitude, and at this point the differential-scattering cross section can vary from 0 to 4 C^4R^2, depending on the value of a. At larger angles, the cross section will be dominated by the term C^4R^2. Because of this interference between the two amplitudes, we have been able to estimate the values of R and a for the two measurements of the K^--p elastic differential-scattering cross section shown in Fig. 6. The method used was similar to the minimization of $\chi^2(A_0, A_1, \gamma, \epsilon)$ as discussed in Sec. V-C, except that in this case we could make a contour map of the χ^2 function, since χ^2 is a function of only the two parameters (R, a). In Table XVI we give the values of R and a that minimize the χ^2 function for the two momentum intervals. The uncertainties were obtained from the contour on which the value of χ^2 differed by 1 from its minimum value.

The small real part of the nuclear amplitude suggested by these values of R and a is in agreement with the large values observed for the total absorption cross sections, and is another indication that the low-momentum K^--p interactions are dominated by very strong absorption processes. The average values of the phase of the nuclear amplitude for the two s-wave zero-effective-range solutions of Sec. V-C are given in Table XVII for comparison.

VI. CONCLUSIONS

There are several absorption channels available to the K^--p system. Couplings to these channels are so strong that they dominate the behavior of the interactions, even the elastic channel. The strong damping introduced by these absorptions gives rise to an elastic cross section resembling the 1/v law expected of an absorption cross section. The elastic nuclear-scattering amplitude is nearly pure imaginary and, therefore, interferes very little with the Coulomb amplitude, which is nearly real.

A simple s-wave zero-effective-range parameterization is adequate to describe the K^--p interaction within the limits of the present data. The angular distributions for K^--p interactions are quite consistent with isotropy, and the s-wave theory seems to fit well. The data of this experiment are probably not sufficiently definitive to justify a fit with more parameters using a nonzero effective-range theory. Three times as much K^--p data as reported here are now available on film, and these data are in the process of being analyzed. This additional information may be sufficient to justify fitting the data to a nonzero-effective-range theory such as the one proposed by Ross and Shaw.[25]

ACKNOWLEDGMENTS

Our experiment would not have been possible without the generous contributions of time and effort on the part of many people. We are particularly indebted to Luis Alvarez, Joseph Murray, Arthur Rosenfeld, Robert Tripp, and Frank Solmitz. We would also like to acknowledge valuable discussions with Richard Dalitz, Robert Glasser, Uli Kruse and Michael Nauenberg. We express our gratitude to Paul Nordin, Jr., and Peter Berge for their help in this collaborative effort of data analysis, and to the Bevatron staff, bubble chamber crew, and the scanners and technicians, whose support was invaluable.

APPENDIX

Maximum-Likelihood Estimate of the Number of Interactions per Momentum Interval

In the analysis of this experiment it was always necessary to consider two types of interactions: those arising from the discrete set of stopped K mesons, and those created by K-p interactions over a continuum of K momenta. Any individual hyperon event cannot be classified unambiguously as one or the other; however, all the events in the experiment taken together can be used to estimate the distribution of events in the two classes. To this end, the number of events in each of several momentum intervals was estimated according to the maximum-likelihood method.[4]

An attempt was made to fit all the hyperon productions as in-flight interactions; however, the kinematics program frequently only gave a fit with zero K momentum. Hence, the measurements of the events also can be divided into two classes corresponding to at-rest fits and in-flight fits. The contributions to the likelihood calculations were different for each class.

Formulation of the Likelihood Problem

The likelihood function is defined as the probability of observing an experimental measurement as a function of the set of parameters a_i to be estimated. The set of parameters that provides the highest probability of observing the experimental results is taken as the best estimate of the parameters. In our particular case, the problem is one of determining the best estimates for the true number of events expected in several momentum intervals. This task is confounded in two ways: first, there is the usual problem of statistical fluctuation; that is, even if one knows the number of events expected, there is a statistical uncertainty in the number observed. Secondly, the momentum of a particle cannot be measured with infinite precision, and therefore, the measured momentum will in general differs from the true momentum, possibly causing the event to be included in an incorrect momentum interval.

More specifically, the probability of observing a certain number of events in a set of momentum intervals is really a compound probability having two important factors. First, there is the probability that there will be an event in the true momentum interval p, p + dp. Secondly, there is the probability that, given such an event, the event should be measured ("observed") in the momentum interval p_δ, $p_\delta + dp_\delta$. This combined probability can be written as

$$d^2P = \left[P_t (p)\, dp \right] \left[P_\delta (p, p_\delta) dp_\delta \right] , \qquad \text{(A-1)}$$

where

P_t = a theoretical expression for the probability of an event at true momentum p, a function of one or more parameters a_i, and

P_δ = the probability that p should be observed as p_δ.

One can then sum over all true p to give the total probability of observing any event in the interval p_δ, $p_\delta + p_\delta$ as

$$dP = \left[\int P_t(p)\, P_{p_0}(p, p_{p_0}) dp \right] dp_{p_0} . \qquad \text{(A-2)}$$

In the particular case of the hyperons, there is (in addition to the continuum of probabilities represented by P_t) a discrete probability representing the probability of an event occurring at rest.

For interactions that give in-flight fits, the differential probability dP for observing an interaction at observed K-momentum p_{p_0} is then given by

$$\frac{dP(a_i)}{dp_{p_0}} = \frac{1}{N_T} \left[\int_0^\infty \frac{dn(a_i)}{dp}\, C(p)\, P_{p_0}(p, \Delta p, p_{p_0}) dp + N_R C(0) P_{p_0}(0, \Delta p, p_{p_0}) \right] . \qquad \text{(A-3)}$$

In the case of the at-rest fits, the probability of seeing an interaction is given by

$$P(a_i) = \frac{1}{N_T} \left\{ \int_0^\infty \frac{dn(a_i)}{dp}\, C(p) \left[1 - \int_{p_{min}}^\infty P_{p_0}(p, \Delta p, p_{p_0}) dp_{p_0} \right] dp \right.$$

$$\left. + N_R\, C(0) \left[1 - \int_{p_{min}}^\infty P_{p_0}(p, \Delta p, p_{p_0}) dp_{p_0} \right] \right\} , \qquad \text{(A-4)}$$

where $\frac{dn(a_i)}{dp}$ = number of events per momentum interval as a function of the parameters a_i .

$C(p)$ = probability of passing acceptance criteria on hyperon length and orientation, assuming a true momentum p,

$P_{p_0}(p, \Delta p, p_{p_0})$ = probability that an event at true momentum p should be observed between momentum p_{p_0} and $p_{p_0} + dp_{p_0}$, given measurement error Δp,

p_{min} = measured momentum, below which an event is considered to fit an at-rest interaction, and

N_R = estimate of the true number of at-rest interactions.

The true total number of acceptable events is then

$$N_T = N_R\, C(0) + \int_0^\infty \frac{dn(a_i)}{dp}\, C(p)dp. \qquad \text{(A-5)}$$

The probability expressed in this way is normalized to unity when one integrates over all observed K-momenta p_o for in-flight fits, and adds in the probability of observing an at-rest fit.

The log of the likelihood function is formed by summing the log of the probability for each event:

$$\ln L = \sum_{i=1}^{N_1} \ln P_i(a_i) + \sum_{j=1}^{N_2} \ln \frac{dP_j(a_i)}{dp_o}\,, \qquad \text{(A-6)}$$

where

N_1 = number of at-rest fits, and

N_2 = number of in-flight fits.

The estimated values of the a_i are then taken as the values that maximize the function ln L.

In practice, $dn(a_i)/dp$ was parameterized by assigning a parameter to each momentum interval considered, so that $dn/dp = a_i$ in the ith interval. The variance matrix was estimated for the parameters on the basis of the formula

$$(V_{ij})^{-1} = -\frac{d^2 \ln L}{da_i\, da_j} = \overline{(\delta a_i\, \delta a_j)}^{-1}\,. \qquad \text{(A-7)}$$

FOOTNOTE AND REFERENCES

*Work done under the auspices of the U. S. Atomic Energy Commission.

1. R. H. Dalitz and S. F. Tuan, Ann. Phys. 10, 307 (1960).

2. T. B. Day, G. A. Snow, and J. Sucher, Phys. Rev. Letters 3, 61 (1950).

3. Luis W. Alvarez, The Interactions of Strange Particles, in Proceedings of the Ninth International Annual Conference on High Energy Physics, Kiev, 1959 (Academy of Sciences, Moscow, 1960).

4. William E. Humphrey, Hyperon Production by K^- Mesons Incident on Hydrogen (Ph. D. Thesis), Lawrence Radiation Laboratory Report UCRL-9752, June 1961 (unpublished).

5. Ronald R. Ross, Elastic-and Charge-Exchange Scattering of K^- Mesons in Hydrogen (Ph. D. Thesis), Lawrence Radiation Laboratory Report UCRL-9749, August 1960 (unpublished).

6. S. C. Freden, C. Gilbert, and R. S. White, Phys. Rev. 118, 564 (1960).

7. D. H. Davis, R. D. Hill, B. D. Jones, V. Sanjeevaiah, J. Zakrzwski, and J. P. Lagraux, Phys. Rev. Letters 6, 132 (1961).

8. J. D. Jackson and H. W. Wyld, Nuovo cimento 13, 85 (1959); Phys. Rev. Letters 2, 355 (1959).

9. Joseph J. Murray, A Coaxial Static-Electromagnetic Velocity Spectrometer for High-Energy Particles, University of California Radiation Laboratory Report UCRL-3492, May 1957 (unpublished).

10. N. Horwitz, J. J. Murray, R. R. Ross, and R. D. Tripp, 450-Mev/c K^- and $\bar{p}$ Beams at the Northwest Target Area of the Bevatron Separated by the Coaxial Velocity Spectrometer, University of California Radiation Laboratory Report UCRL-8269, June 1958 (unpublished).

11. H. A. Bethe, Phys. Rev. 89, 1256 (1953).

12. Walter H. Barkas and Arthur H. Rosenfeld, Data for Elementary-Particle Physics, University of California Radiation Laboratory Report UCRL-8030, March 20, 1958 (unpublished).

13. M. Gell-Mann and A. H. Rosenfeld, Ann. Rev. Nuclear Sci. 7, 407 (1957).

14. B. Cork, L. Kerth, W. A. Wenzel, J. W. Cronin, and R. W. Cool, Phys. Rev. 120, 1000 (1960).

15. P. Franzini, A. Garfinkel, J. Keren, A. Michelini, R. Plano, A. Prodell, M. Schwartz, J. Steinberger, and S. E. Wolf, Bull. Am. Phys. Soc. 5, 224 (1960).

16. A. Pais, On the Theory of Non-Leptonic Hyperon Decays, Lawrence Radiation Laboratory Report UCRL-9460, October 1960 (unpublished).

17. S. P. Rosen, Phys. Rev. Letters 6, 504 (1961).

18. Frank S. Crawford, Jr., Marcello Cresti, Myron L. Good, M. Lynn Stevenson, and Harold K. Ticho, Phys. Rev. Letters 2, 114 (1959).

19. F. Eisler, R. Plano, A. Prodell, N. Samios, M. Schwartz, J. Steinberger, P. Bassi, V. Borrelli, G. Puppi, H. Tanaka, P. Waloschek, V. Zoboli, M. Conversi, P. Franzini, I. Manelli, R. Santangelo, V. Silvestrini, G. L. Brown, D. A. Glaser, and C. Graves, Nuovo cimento 7, 222 (1958).

20. Jack Leitner, Paul Nordin, Jr., Arthur H. Rosenfeld, Frank T. Solmitz, and Robert D. Tripp, Phys. Rev. Letters 3, 238 (1959).

21. R. Gatto, private communication, October 28, 1959.

22. J. D. Jackson, D. G. Ravenhall, and H. W. Wyld, Nuovo cimento 9, 834 (1958).

23. R. H. Dalitz, Strange-Particle Interactions, in Proceedings of the 1958 Annual International Conference on High-Energy Physics (CERN, Geneva, 1959), pp. 187-201.

24. R. H. Dalitz, On the Strong Interactions of the Strange Particles, Lawrence Radiation Laboratory Report UCRL-9580, January 1961 (unpublished).

25. Marc H. Ross and Gordon L. Shaw, Annals of Physics 9, 391 (1960) and 13, 147 (1961). These authors have applied their general theory on multichannel effective range to the K^--p system (private communication).

Table I. Momentum dependence of the elastic-scattering cross section ($1.0 \leq \cos \theta_{c.m.} \leq 0.966$).

K^- lab momentum interval (Mev/c)	Experimental cross section estimate (mb)	Variance matrix for estimate of cross section						
		100-125	125-150	150-175	175-200	200-225	225-250	250-275
100-125	139.6	564.2						
125-150	90.0	-10.2	223.0					
150-175	101.3	- 0.4	- 6.2	150.3				
175-200	71.3	- 0.6	- 0.1	- 3.4	73.2			
200-225	47.4	- 0.5	- 0.2	- 0.3	-1.4	41.2		
225-250	39.2	- 0.5	- 0.4	- 0.4	-0.6	-0.7	49.4	
250-275	44.2	- 0.6	- 0.5	- 0.5	-0.3	-0.1	-2.7	255.6

The symmetric elements of the variance matrix ($\overline{\delta\sigma_i \delta\sigma_j}$) have not been duplicated.

Table II. Momentum dependence of the charge-exchange scattering cross section.

K^- lab momentum interval (Mev/c)	Experimental cross section estimates (mb)	Variance matrix for estimate of cross section						
		89-125	125-150	150-175	175-200	200-225	225-250	250-275
89-125	28.4	470.0			The symmetric elements of the variance matrix $(\overline{\delta\sigma_i \delta\sigma_j})$ have not been duplicated.			
125-150	19.0	-53.6	202.5					
150-175	20.4	4.0	-16.2	125.2				
175-200	13.2	- 0.4	1.4	-11.2	54.1			
200-225	13.8	0.0	- 0.1	0.6	-4.6	47.1		
225-250	19.4	0.0	0.0	- 0.3	0.0	-10.8	81.4	
250-275	0	0.0	0.0	0.0	0.0	0.0	0.0	144.5

Table III. Momentum dependence of the Σ^- cross section.

K^- lab momentum interval (Mev/c)	Experimental cross section estimate (mb)	Variance matrix for estimate of cross section								
		50-75	75-100	100-125	125-150	150-175	175-200	200-225	225-250	250-275
50-75	217.5	9499.8								
75-100	110.3	-1088.6	1774.2							
100-125	42.0	32.7	-121.9	416.7						
125-150	48.3	2.0	-1.2	-95.4	226.8					
150-175	10.7	-0.1	-0.3	6.5	-20.7	43.3				
175-200	35.7	-0.6	-0.2	- 0.5	1.5	-11.6	63.4			
200-225	15.8	-0.3	-0.2	0.0	- 0.3	1.7	-12.7	32.3		
225-250	10.4	-0.2	00.1	- 0.1	0.0	- 0.4	3.2	-10.7	30.9	
250-275	17.3	-0.5	-0.2	- 0.1	- 0.2	0.2	- 1.9	6.0	-22.0	138.8

The symmetric elements of the variance matrix $(\overline{\delta\sigma_i \delta\sigma_j})$ have not been duplicated.

Table IV. Momentum dependence of the Σ^+ cross section.

K^- lab momentum interval (Mev/c)	Experimental cross section estimate (mb)	Variance matrix for estimate of cross section							
		75-100	100-125	125-150	150-175	175-200	200-225	225-250	250-275
75-100	27.8	754.0							
100-125	75.8	-202.2	739.6						
125-150	20.8	27.7	-159.0	237.6					
150-175	39.1	-4.9	17.0	-56.5	122.2				
175-200	20.6	0.4	- 3.0	4.8	-18.3	55.4			
200-225	18.2	-0.1	0.2	- 0.7	2.7	-12.0	33.6		
225-250	21.3	-0.1	- 0.2	0.1	- 0.6	1.7	-9.1	46.8	
250-275	15.3	-0.1	- 0.1	- 0.1	0.1	- 0.5	3.1	-22.9	140.9

The symmetric elements of the variance matrix $(\overline{\delta\sigma_i \delta\sigma_j})$ have not been duplicated.

UCRL-10018

Table V. Momentum dependence of the (Σ^0 + Λ) cross section.

K^- lab momentum interval (Mev/c)	Experimental cross section estimate (mb)	Variance matrix for estimate of cross section				
		125-150	150-175	175-200	200-225	225-250
125-150	154.7	32864.2				
150-175	86.7	-18324.2	12174.1			
175-200	11.2	5981.4	-4512.0	2262.8		
200-225	34.6	-1737.6	1443.2	-920.1	557.2	
225-250	5.4	626.4	-534.5	361.5	-245.2	161.5

The symmetric elements of the variance matrix $(\overline{\delta\sigma_i \delta\sigma_j})$ have not been duplicated.

Table VI. Path length and number of events used in calculating cross section and at-rest ratios. (The term "No. Analyzed" refers to the actual number of events analyzed after culling by using selection criteria. The "Final Estimate" denotes our estimate of the true number of events in the experiment, arrived at by making maximum-likelihood adjustments and correcting for culling and neutral decay modes.)

K^- lab momentum	At rest	50-75	75-100	100-125	125-150	150-175	175-200	200-225	225-250	250-275
Path length										
Path length (m)	--	16.12	39.48	78.40	136.79	221.54	316.25	385.98	285.10	80.83
Elastic scattering ($-1.0 \leq \cos\theta_{c.m.} \leq 0.966$)										
No. analyzed	--	4	9	39	39	77	73	65	39	12
Final estimate	--	--	--	38.3	43.1	78.5	78.9	64.1	39.1	12.5
Charge exchange										
No. analyzed	--	--	--	2[a]	3	3	5	6	5	0
Final estimate	--	--	--	10.0[a]	9.1	15.8	14.6	18.6	19.4	0
Σ^-										
No. analyzed	1101.1	7	14	12	14	10	24	16	9	5
Final estimate	1553.3	12.3	15.2	11.5	23.1	8.3	39.5	21.3	10.4	4.9
Σ^+										
No. analyzed	477	6	5	12	11	18	12	18	15	4
Final estimate	721.7	--	3.8	20.8	9.9	30.3	22.8	24.6	21.3	4.3

Table VI. (continued)

K^- lab momentum	At rest	50-75	75-100	100-125	125-150	150-175	175-200	200-225	225-250	250-275
					$\Sigma^0 + \Lambda$					
No. analyzed 471	--	6	60	123	67	34	22	10	11	0
Final estimate 1199.8	--	--		--	74.0	67.2	12.4	46.8	5.4	0.0

[a]The first interval for the charge-exchange scattering is for a K^- lab momentum interval from 89 to 125 Mev/c. The path length for this interval was 100 m.

Table VII. Decay angular distributions.

Decay mode	Angle	Interval widths	$N = a_1 + a_2 \cos\theta + a_3 \cos^2\theta$[a]				Degrees of freedom	χ^2
			a_1	a_2	a_3	a_3/a_1		
$\Sigma^- \rightarrow \pi^- + n$	$\Sigma^- - \pi$	0.2	108.6±5.0	-4.2±5.7	-2.3±11.3	-0.02±0.10	7	3.6
$\Sigma^+ \rightarrow \pi^+ + n$	$\Sigma^+ - \pi$	0.2	20.0±2.3	-2.7±2.6	6.5±5.2	0.33±0.29	7	13.6
$\Sigma^+ \rightarrow \pi^0 + p$	$\Sigma^+ - \pi$	0.2	26.6±2.4	-4.4±2.7	-6.6±5.4	-0.25±0.19	7	7.8
$\Sigma^+ \rightarrow \begin{matrix}\pi^+ + n \\ \pi^0 + p\end{matrix}$	$\Sigma^+ - \pi$	0.2	48.0±3.3	-6.9±3.8	-2.4±7.5	-0.05±0.16	7	9.1
$\Lambda \rightarrow \pi^- + p$ Direct	$\Lambda - \pi$	0.2	8.1±1.3	2.9±1.6	-0.6±3.1	-0.07±0.37	7	10.0
$\Lambda \rightarrow \pi^- + p$ Indirect	$\Lambda - \pi$	0.2	38.4±3.0	3.3±3.4	-0.5±6.7	-0.01±0.17	7	8.2
$\Sigma^0 \rightarrow \gamma + \Lambda$ (Fig. 13)	$\Sigma^0 - \gamma$	2 Mev	34.5±2.7	0.6±3.0	0.3±6.1	0.01±0.18	8	2.9

[a] N = Number/interval, where the interval width is given in the table for each case.

Table VIII. Summary of lifetime calculations.

Times (10^{-10} sec)	Σ^-	Σ^+	Λ
t_c	0.226	0.216	event-dependent
t_m	2.553	3.024	event-dependent
N_1	940	445	799
N_2	268	11	———
L_1 lifetime calculation	1.58±0.06	0.765±0.04	———
L_2 lifetime calculation	1.63±0.13	0.755±0.05	2.69±0.11
Best lifetime estimate	1.58±0.06	0.765±0.04	2.69±0.11

Table IX. Physical measurements contributing to the determination of the s-wave zero-effective-range parameters.

a	Physical quantity measured σ_{aj}^{m}	$a_a \leq j \leq b_a$		No. of measurements	Total range of K^- lab momentum (Mev/c)
		a_a	b_a		
1	$\int_{-1.00}^{0.85} \frac{d\sigma_{el}}{d\Omega} d\Omega$	5	11	7	100-275
2	$\int_{0.85}^{0.90} \frac{d\sigma_{el}}{d\Omega} d\Omega$	5	11	7	100-275
3	$\int_{0.90}^{0.95} \frac{d\sigma_{el}}{d\Omega} d\Omega$	5	11	7	100-275
4	$\int_{0.95}^{0.966} \frac{d\sigma_{el}}{d\Omega} d\Omega$	5	11	7	100-275
5	$\sigma(K^- + p \to \bar{K}^0 + n)$	5	11	7	100-275
6	$\sigma(K^- + p \to \Sigma^- + \pi^+)$	3	11	9	150-275
7	$\sigma(K^- + p \to \Sigma^+ + \pi^-)$	4	11	8	75-275
8	$\sigma(K^- + p \to \Sigma^0 + \pi^0) + \sigma(K^- + p \to \Lambda + \pi^0)$	6	10	5	125-250
9	$\frac{\sigma(K^- + p \to \Lambda + \pi^0)}{\sigma(K^- + p \to \Lambda + \pi^0) + \sigma(K^- + p \to \Sigma^0 + \pi^0)}$	7	10	4	150-250
10	$\frac{\Gamma(K^- + p \to \Lambda + \pi^0)}{\Gamma(K^- + p \to \Lambda + \pi^0) + \Gamma(K^- + p \to \Sigma^0 + \pi^0)}$	0	0	1	At rest

Table IX. Continued

a	Physical quantity measured σ^{m}_{aj}	$a_a \leq j \leq b_a$		No. of measurements	Total range of K^- lab momentum (Mev/c)
		a_a	b_a		
11	$\frac{\Gamma(K^- + p \rightarrow \Sigma^- + \pi^+)}{\Gamma(K^- + p \rightarrow \Sigma^+ + \pi^-)}$	0	0	1	At rest
12	$\frac{\Gamma(K^- + p \rightarrow \Sigma^- + \pi^+) + \Gamma(K^- + p \rightarrow \Sigma^+ + \pi^-)}{\Gamma(K^- + p \rightarrow \Sigma^0 + \pi^0) + \Gamma(K^- + p \rightarrow \Lambda + \pi^0)}$	0	0	1	At rest
				64 Total	

Table X. Scattering-length parameters that best fit the data, and their starting values.

	Solution	a_0 (f)	b_0 (f)	a_1 (f)	b_1 (f)	γ	ϵ	χ^2	Probability of exceeding χ^2
Starting values	a^-	-0.75	2.00	-0.85	0.21	2.15	0.41	92.44	0.003
	b^+	1.15	2.00	0.70	0.25	2.15	0.41	103.33	0.0002
Final values	1	-0.220	2.742	0.029	0.384	2.153	0.403	57.914	0.48
Starting values	a^+	0.05	1.10	1.45	0.35	2.15	0.41	120.78	< 0.00001
	b^-	-1.85	1.10	-0.10	0.65	2.15	0.41	128.10	< 0.00001
Final values	2	-0.592	0.964	1.202	0.562	2.086	0.396	73.494	0.083

Table XI. Properties of the χ^2 space in the vicinity of Solution 1.

Parameters	$a_{0(f)}$	$b_{0(f)}$	$a_{1(f)}$	$b_{1(f)}$	γ	ϵ
Central values	-0.220	2.748	0.029	0.384	2.153	0.403
Uncertainties of central values	1.07	0.31	0.33	0.085	0.16	0.037

Variance matrix $\underline{V}$ ($V_{ij} = \overline{\delta\beta_i \, \delta\beta_j}$)

a_0	1.15			Symmetric elements of the matrix $\underline{V}$ have not been duplicated.		
b_0	0.12	0.099				
a_1	0.28	0.033	0.11			
b_1	-0.051	-0.0092	-0.0090	0.0056		
γ	-0.052	0.0074	-0.011	-0.00065	0.027	
ϵ	-0.0098	0.00032	-0.0012	-0.00016	-0.00028	0.00072

Expansion matrix $\underline{D}$ ($\chi^2 \approx \sum_{i,j} \Delta\beta_i \, \underline{D}_{ij} \, \Delta\beta_j + 57.91$)

a_0	12.13			Symmetric elements of the matrix $\underline{D}$ have not been duplicated.		
b_0	-0.10	25.91				
a_1	-24.25	-6.24	73.67			
b_1	74.82	29.92	-116.52	926.21		
γ	-4.45	-9.26	22.62	-9.13	85.85	
ϵ	136.58	-20.80	-214.51	991.50	14.65	4471.0

UCRL-10018

Table XII. Properties of the χ^2 space in the vicinity of Solution 2.

Parameters	a_0 (f)	b_0 (f)	a_1 (f)	b_1 (f)	γ	ϵ
Central values	-0.592	0.964	1.202	0.562	2.04	0.391
Uncertainties of central values	0.46	0.17	0.060	0.15	0.18	0.023

Variance matrix $\underline{V}$ ($V_{ij} = \overline{\delta\beta_i \, \delta\beta_j}$)

a_0	0.21					
b_0	0.12	0.028				
a_1	-0.11	-0.0053	0.0036			
b_1	-0.051	0.0038	0.037	0.022		
γ	0.043	-0.0028	-0.0041	0.012	0.033	
ϵ	-0.00049	0.00032	0.00073	-0.00092	0.00061	0.00054

Symmetric elements of the matrix $\underline{V}$ have not been duplicated.

Expansion matrix $\underline{D}$ ($\chi^2 \approx \sum_{ij} \Delta\beta_i \, \underline{D}_{ij} \, \Delta\beta_j + 73.49$)

a_0	41.55					
b_0	-40.74	139.44				
a_1	-42.25	129.38	102.14			
b_1	111.93	-100.92	-55.79	299.93		
γ	0.58	16.61	-7.93	11.59	57.50	
ϵ	258.58	-317.43	-184.09	609.90	-24.32	5022.5

Symmetric elements of the matrix $\underline{D}$ have not been duplicated.

Table XIII. Properties of Solution 1

($A_0 = -0.22 + i2.74$, $A_1 = 0.02 + i0.38$, $\gamma = 2.153$, $\varepsilon = 0.402$, $\chi^2 = 57.9$)

K^- lab momentum (Mev/c)	Cross sections (mb)							Production ratios			Phase
	σ_{el}	σ_{ce}	σ_0	σ_1	σ_{Σ^-}	σ_{Σ^+}	$\sigma_{\Sigma^0+\Lambda}$	$\frac{A}{\Sigma^0+\Lambda}$	$\frac{\Sigma^-}{\Sigma^+}$	$\frac{(\Sigma^-+\Sigma^+)}{(\Sigma^0+\Lambda)}$	$\phi_{\Sigma_0-\Sigma_1}$
At rest	-	-	-	-	-	-	-	0.21	2.15	1.89	60.3
37.5	1374.3	0.0	2178.9	425.4	567.4	286.0	448.8	0.19	1.98	1.90	62.4
62.5	356.2	0.0	1000.5	171.5	242.9	141.9	201.3	0.17	1.71	1.91	67.3
87.5	201.3	0.0	594.5	83.1	122.6	100.4	115.8	0.14	1.22	1.93	80.9
112.5	122.6	27.1	278.5	86.4	55.8	62.8	63.8	0.27	0.89	1.86	94.1
137.5	92.6	23.6	172.9	71.1	37.3	41.5	43.1	0.33	0.90	1.83	93.4
162.5	74.7	19.4	117.2	58.8	26.9	29.7	31.4	0.38	0.91	1.81	93.0
187.5	62.5	15.8	84.0	49.4	20.4	22.4	23.9	0.42	0.91	1.79	92.7
212.5	53.6	13.0	62.7	42.1	16.0	17.5	18.9	0.45	0.92	1.77	92.5
237.5	46.8	10.8	48.4	36.4	13.0	14.0	15.4	0.48	0.92	1.75	92.3
262.5	41.4	9.1	38.3	31.7	10.7	11.5	12.8	0.50	0.93	1.74	92.1
287.5	37.1	7.7	30.9	28.0	9.0	9.7	10.8	0.52	0.93	1.73	92.0

Table XIV. Properties of Solution 2

($A_0 = -0.59 + i0.96$, $A_1 = 1.20 + i0.56$, $A_\gamma = 2.04$, $\epsilon = 0.39$, $\chi^2 = 73.5$).

K^- lab momentum (Mev/c)	Cross sections (mb)							Production ratios			Phase
	σ_{el}	σ_{ce}	σ_0	σ_1	σ_{Σ^-}	σ_{Σ^+}	$\sigma_{\Sigma^0+\Lambda}$	$\frac{\Lambda}{\Sigma^0+\Lambda}$	$\frac{\Sigma^-}{\Sigma^+}$	$\frac{(\Sigma^-+\Sigma^+)}{(\Sigma^0+\Lambda)}$	$\phi_{\Sigma_0-\Sigma_1}$
At rest	-	-	-	-	-	-	-	0.21	2.04	1.91	-63.2
37.5	1210.3	0.0	1451.9	371.0	409.2	187.7	314.6	0.23	2.18	1.90	-61.7
62.5	239.7	0.0	653.3	194.4	197.0	79.9	146.9	0.26	2.46	1.89	-59.0
87.5	115.8	0.0	331.8	157.6	122.4	36.2	86.1	0.36	3.38	1.84	-53.7
112.5	97.5	27.0	184.3	119.9	66.4	31.5	54.2	0.43	2.11	1.81	-68.4
137.5	82.9	24.5	130.0	86.2	42.3	27.3	38.5	0.44	1.55	1.81	-77.1
162.5	73.1	20.4	96.9	64.5	29.0	23.0	28.8	0.44	1.26	1.81	-83.2
187.5	65.6	16.7	75.0	49.8	20.8	19.4	22.3	0.44	1.07	1.81	-88.0
212.5	59.4	13.7	59.7	39.4	15.4	16.5	17.7	0.44	0.93	1.81	-92.0
237.5	54.2	11.3	48.6	31.8	11.8	14.1	14.3	0.43	0.83	1.81	-95.4
262.5	49.7	9.3	40.3	26.1	9.2	12.2	11.8	0.43	0.75	1.81	-98.4
287.5	45.8	7.8	33.9	21.7	7.3	10.6	9.9	0.43	0.69	1.81	-100.9

Table XV. Contributions of the different physical measurements to the final value of χ^2 for Solutions 1 and 2 of Table X

a	Number of measurements	Solution 1 χ^2	Solution 2 χ^2
1	7	7.56	15.21
2	7	2.66	3.73
3	7	1.79	1.91
4	7	3.93	3.49
5	7	2.14	2.20
6	9	9.31	11.80
7	8	10.76	7.21
8	5	13.19	15.39
9	4	6.28	9.28
10	1	0.27	2.27
11	1	0.00	0.88
12	1	0.02	0.11
Total	64	57.91	73.49

Table XVI. Values of the modulus and phase of the nuclear part of the elastic-scattering amplitude as determined from the elastic-differential-scattering cross sections in Fig. 6.

K^- lab momentum interval (Mev/c)	R (f)	a (deg)	Ra correlation	C^2
100-175	0.81±0.06	78±31	+0.84	1.085
175-250	0.62±0.04	97±38	+0.78	1.058

Table XVII. Average phase of the nuclear amplitude calculated from the s-wave zero-effective-range parameters of Solutions 1 and 2, and the phase obtained from the differential-scattering cross sections of Fig. 6.

Solution	a (deg)	
	(100-175 Mev/c)	(175-250 Mev/c)
1	91	90
2	75	78
Experimental (Table XVI)	78±31	97±38

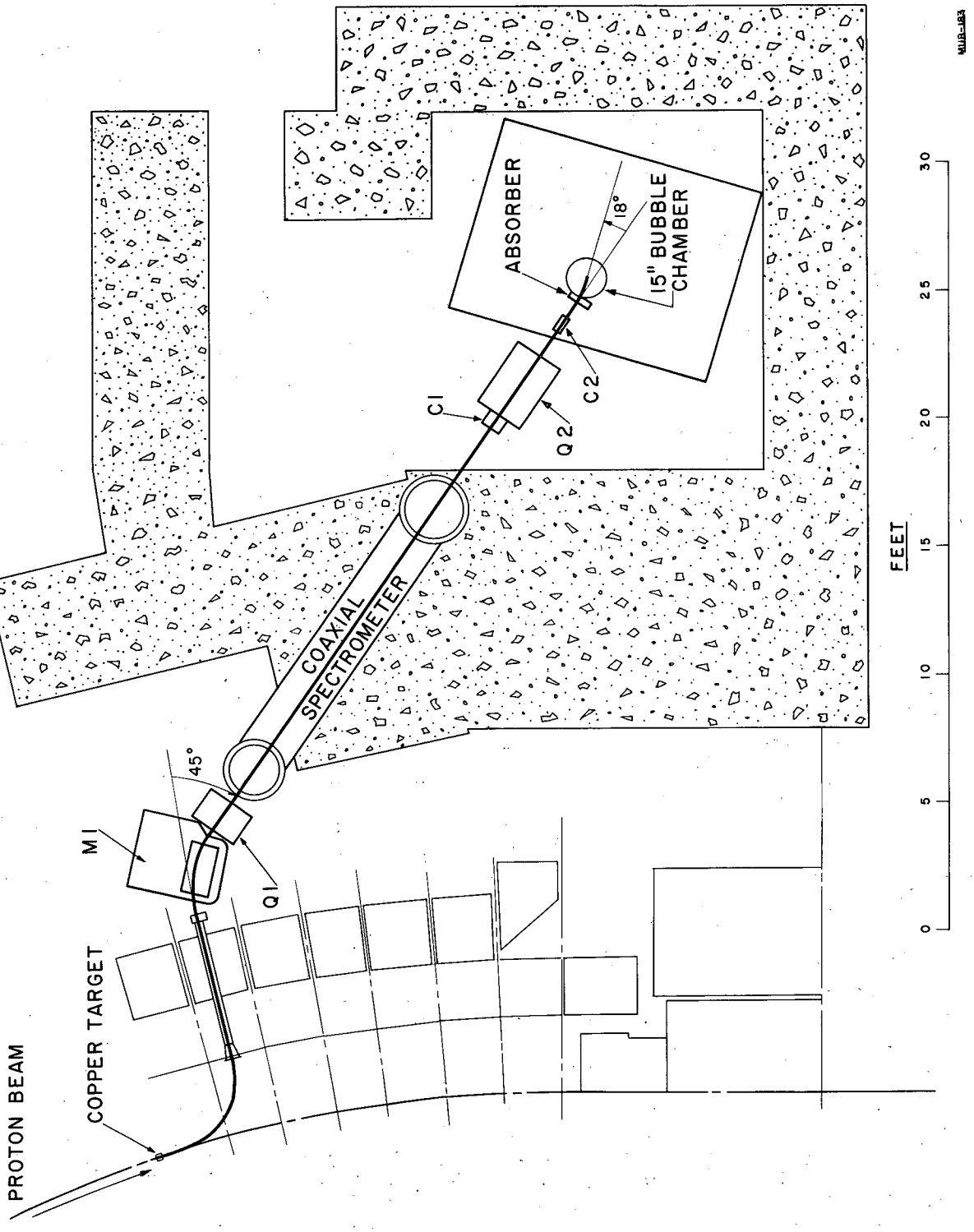

Fig. 1. Schematic diagram of the 450-Mev/c K^- beam at the northwest target area of the Berkeley Bevatron.

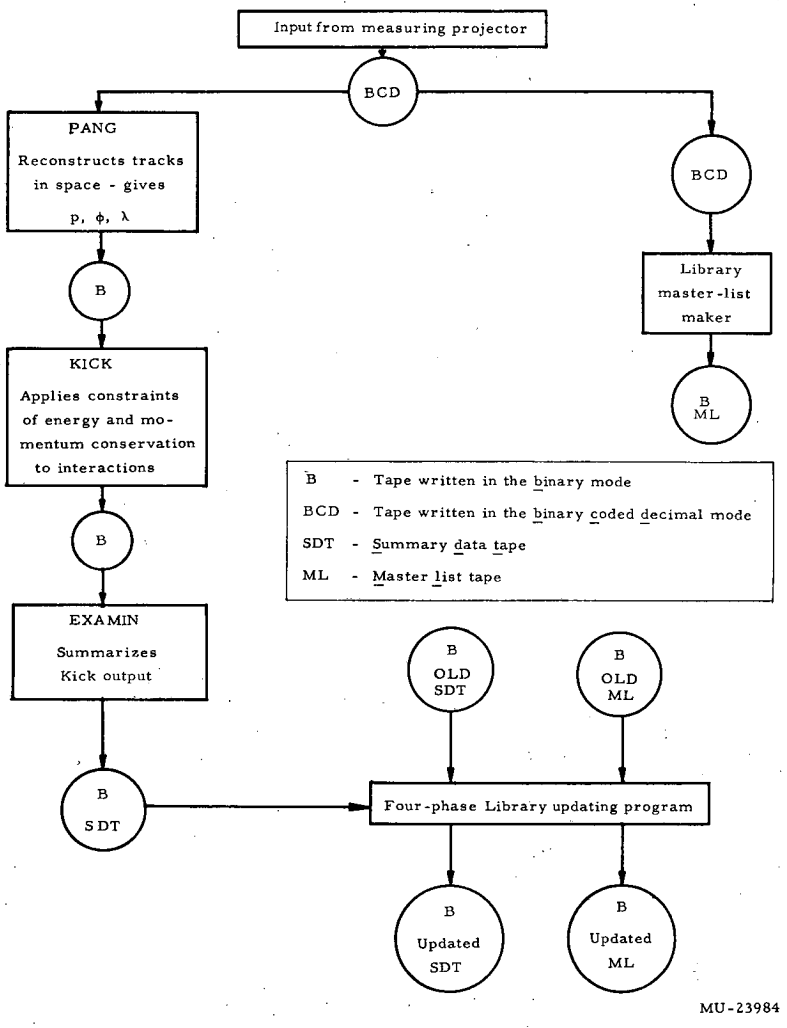

Fig. 2. Block diagram of the system of computer programs used for the analysis of K^--p interactions in this experiment.

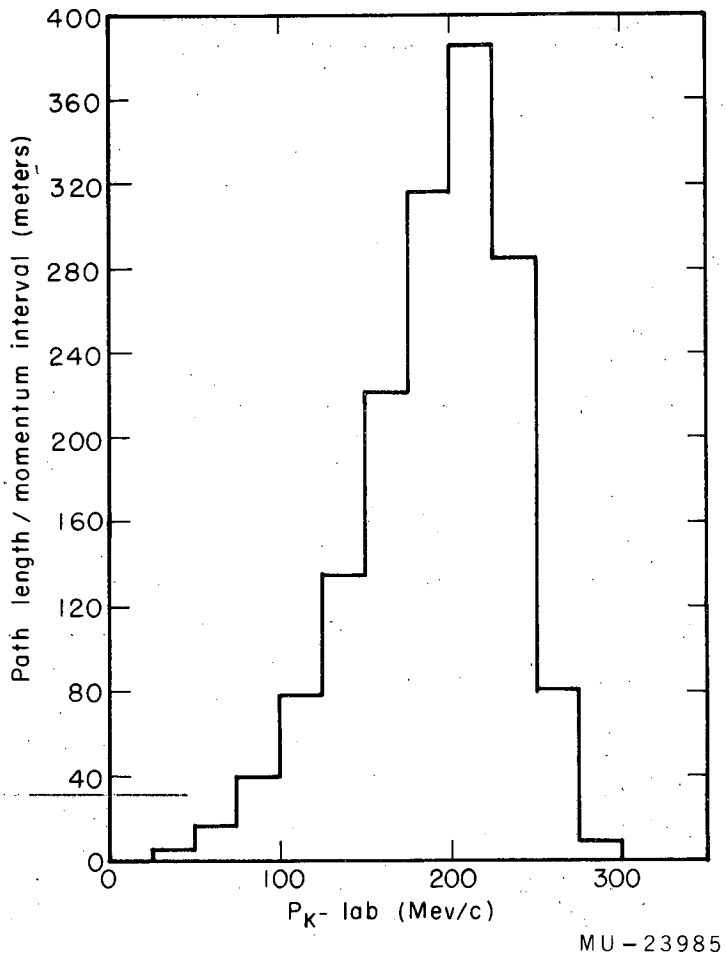

Fig. 3. Histogram of K^- path length as a function of K^- lab momentum.

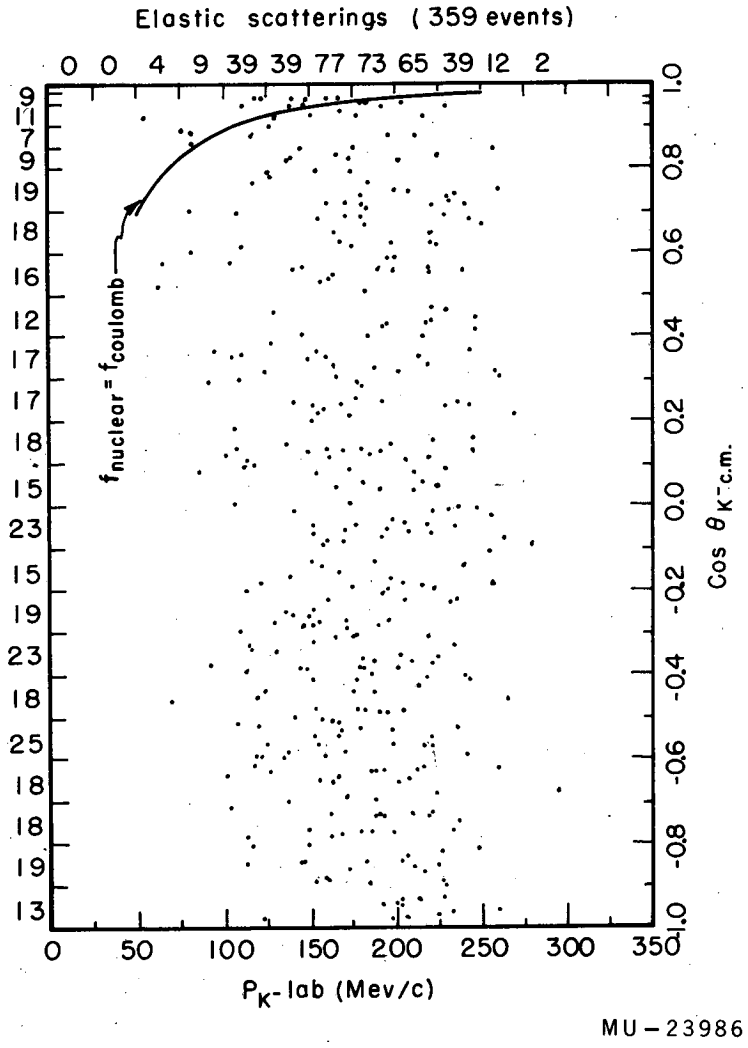

Fig. 4. Scatter plot of observed elastic scatterings that satisfy the selection criteria applied. No selection criteria are applied to events with cos $\theta_{c.m.} > 0.85$. The numbers of events in both momentum and cos θ bands are indicated on the sides opposite the scales.

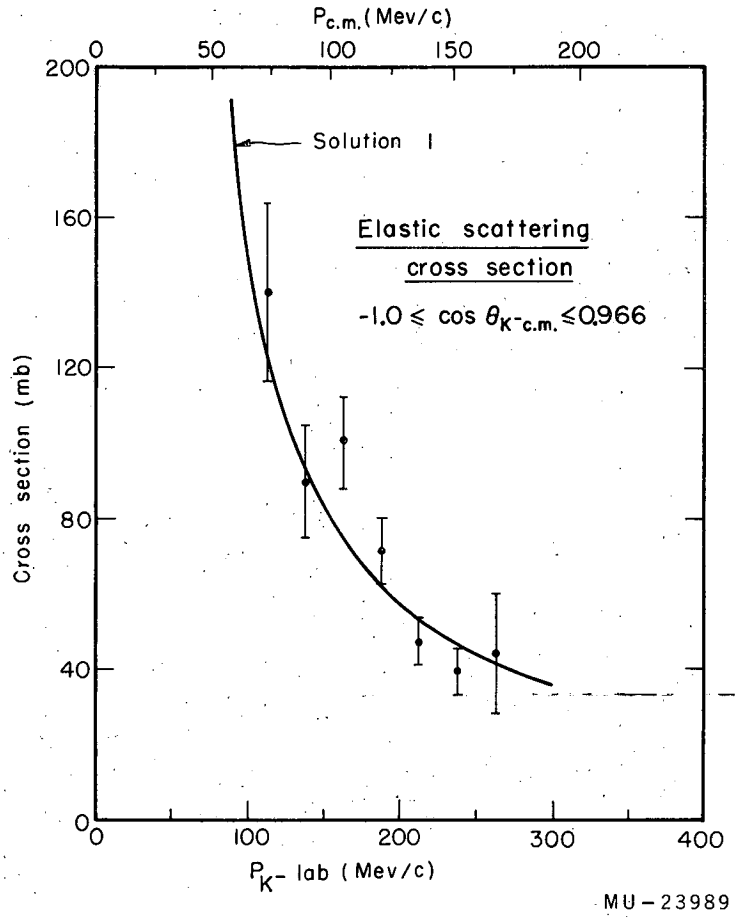

Fig. 5. Total K^--p elastic-scattering cross section for $\cos \theta_{K^- c.m.}$ between -1.0 and 0.966 as a function of K^- lab momentum. The solid curve is the integral of Eq. (15) from -1.0 to 0.966 in $\cos \theta_{K^- c.m.}$, for the scattering lengths of Solution 1 (Table XIII).

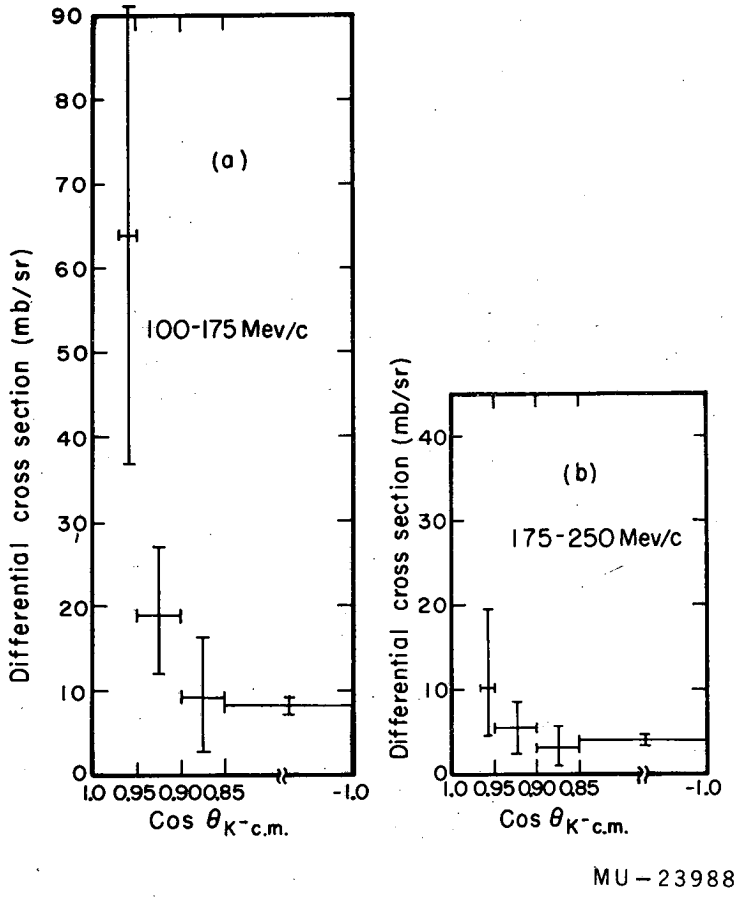

Fig. 6. Elastic K^--p differential scattering cross section for (a) $100 \leq P_{K^-lab} \leq 175$ Mev/c, and (b) $175 < P_{K^-lab} \leq 250$ Mev/c.

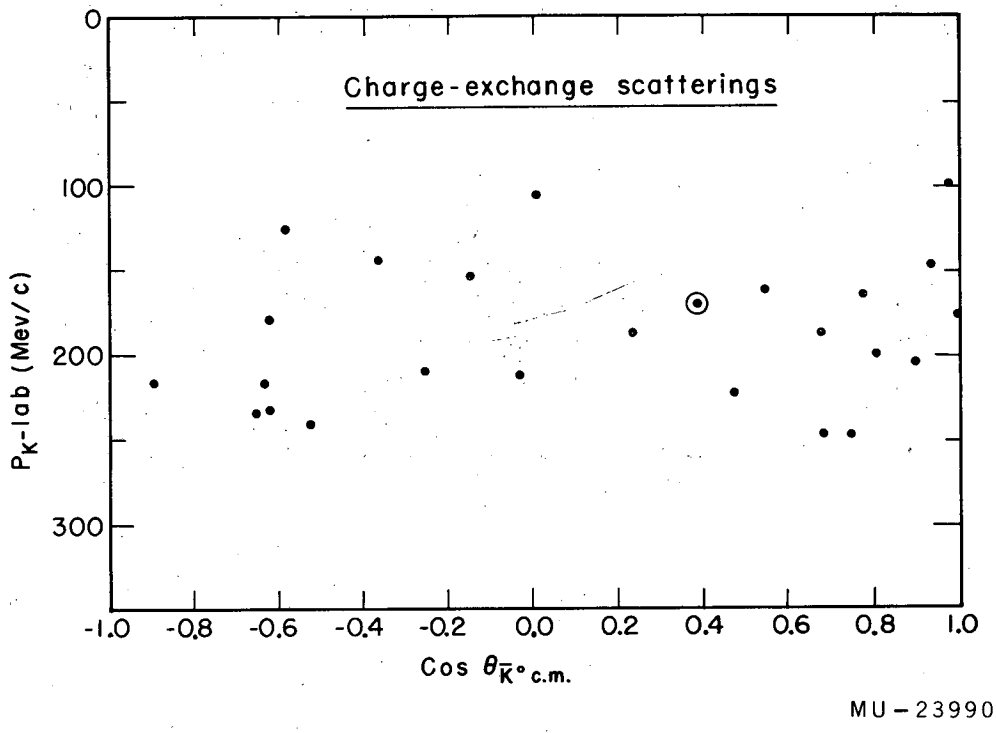

Fig. 7. Scatter plot of $\overline{K}^0$-n production events with K_1^0 decays. The circled event has a $\overline{K}^0$ length less than 1 mm.

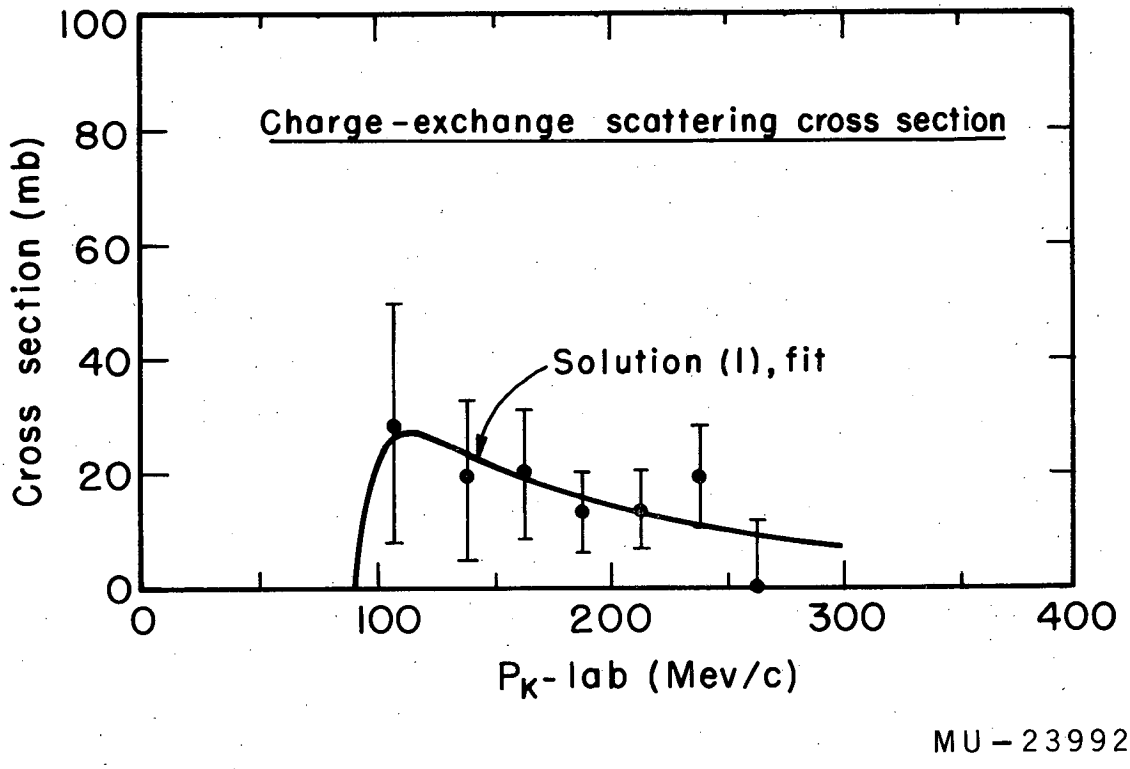

Fig. 8. The K^--p charge-exchange scattering cross section as a function of K^- lab momentum. The solid curve is a graph of Eq. (16) for the scattering lengths of Solution 1 (Table XIII).

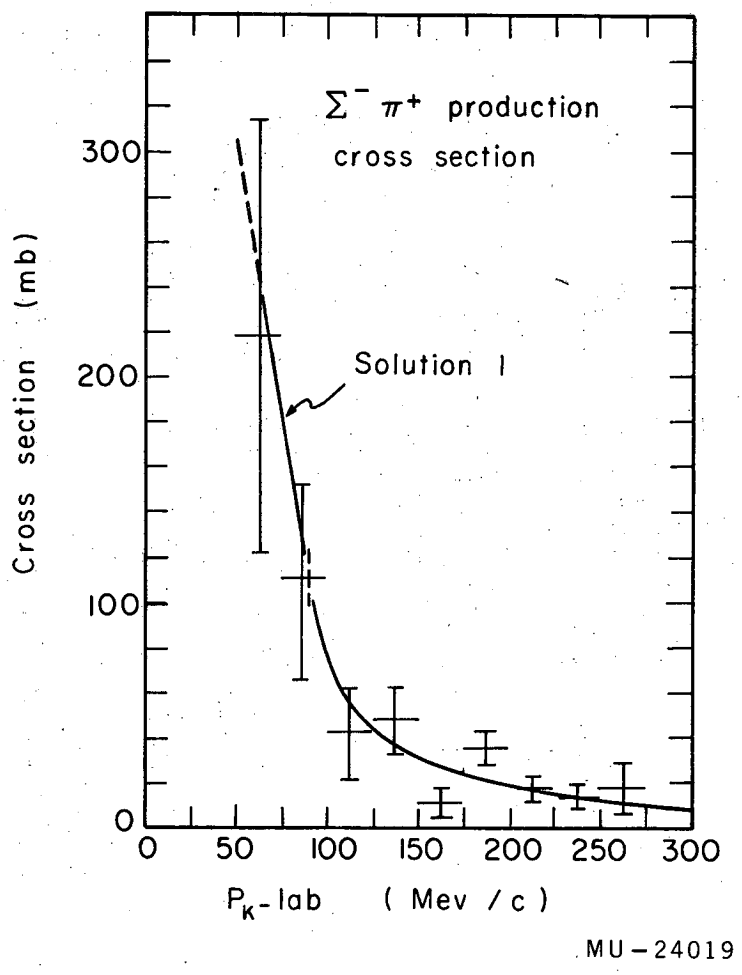

Fig. 9. Cross section for production of Σ^- hyperons presented as a function of the K^- lab momentum. The solid curve represents the theoretical prediction for the better of the two scattering-length solutions (Solution 1, Table XIII).

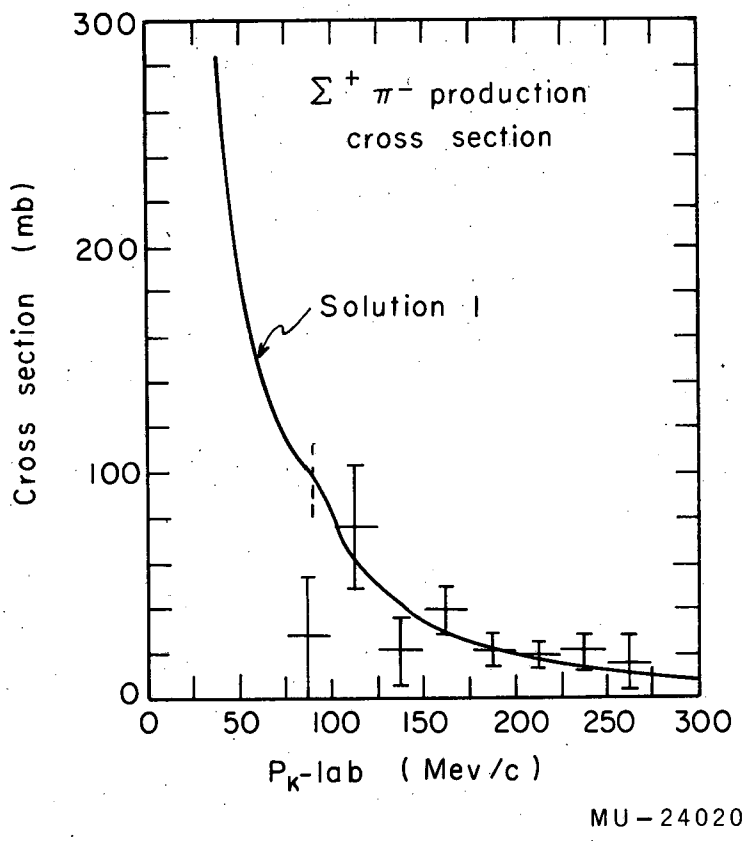

Fig. 10. Cross section for production of Σ^+ hyperons presented as a function of the K^-lab momentum. The solid curve represents the theoretical prediction for the better of the two scattering length solutions (Solution 1, Table XIII).

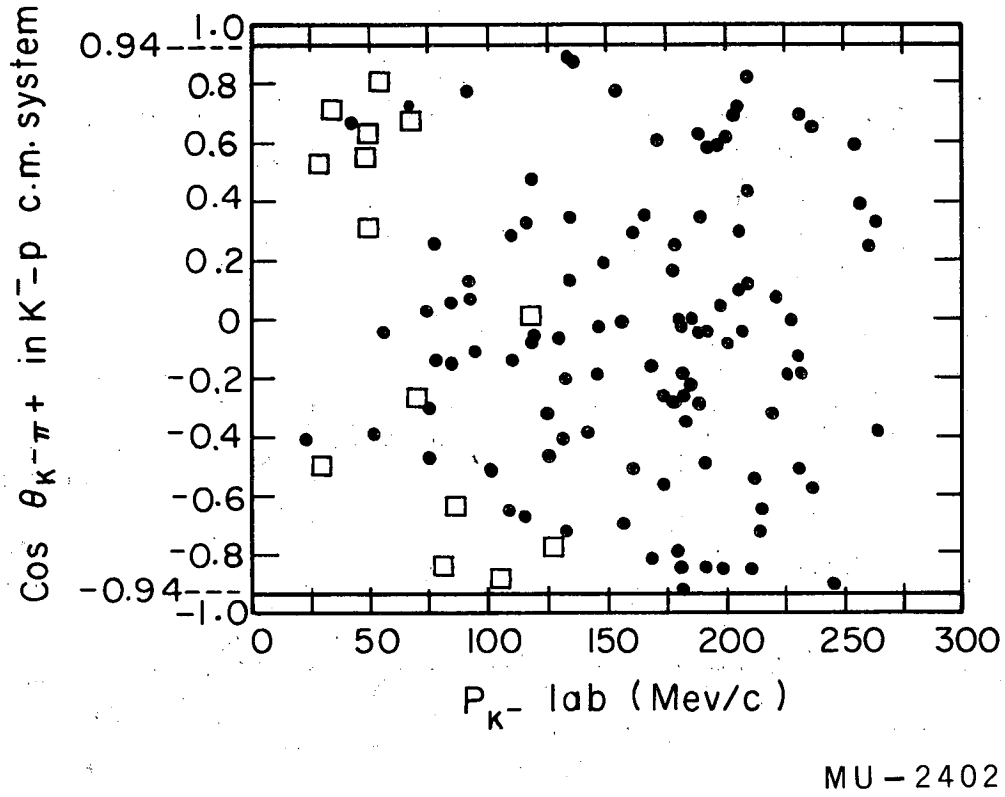

Fig. 11. Scatter plot of $\Sigma^- \pi^+$ in-flight events. Events that are not-in-flight by inspection are indicated by a square (these events have fitted momenta which are at least three standard deviations from stopping).

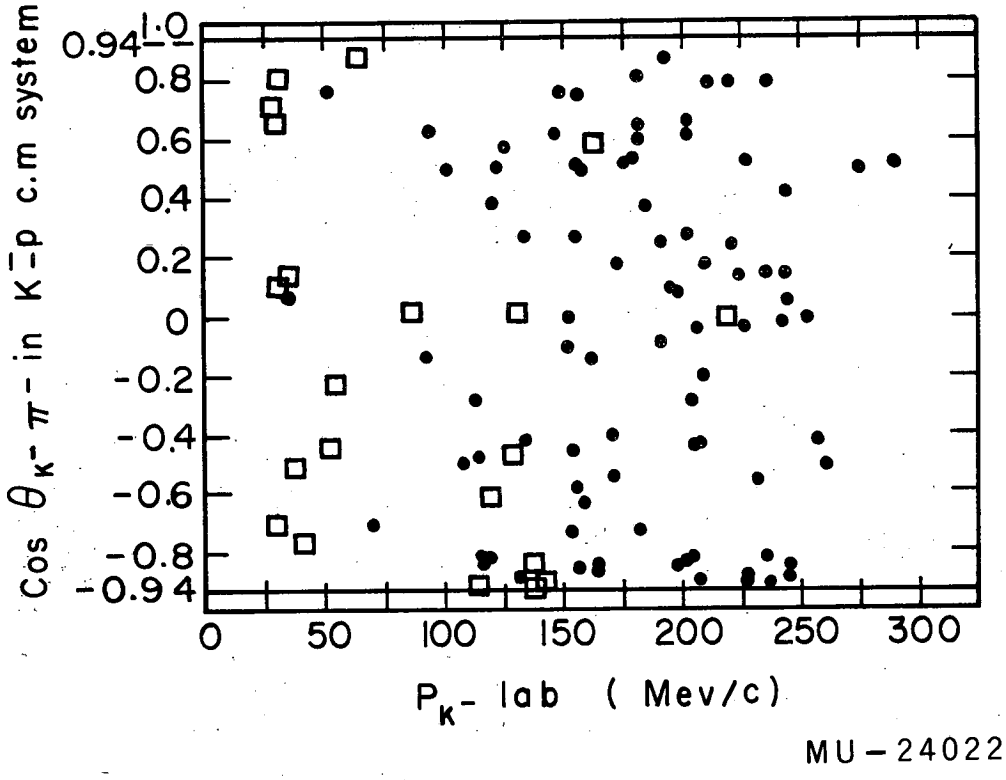

Fig. 12. Scatter plot of $\Sigma^+ \pi^-$ in-flight events. Events that are not in-flight by inspection are indicated by a square (these events have fitted momenta which are at least three standard deviations from stopping).

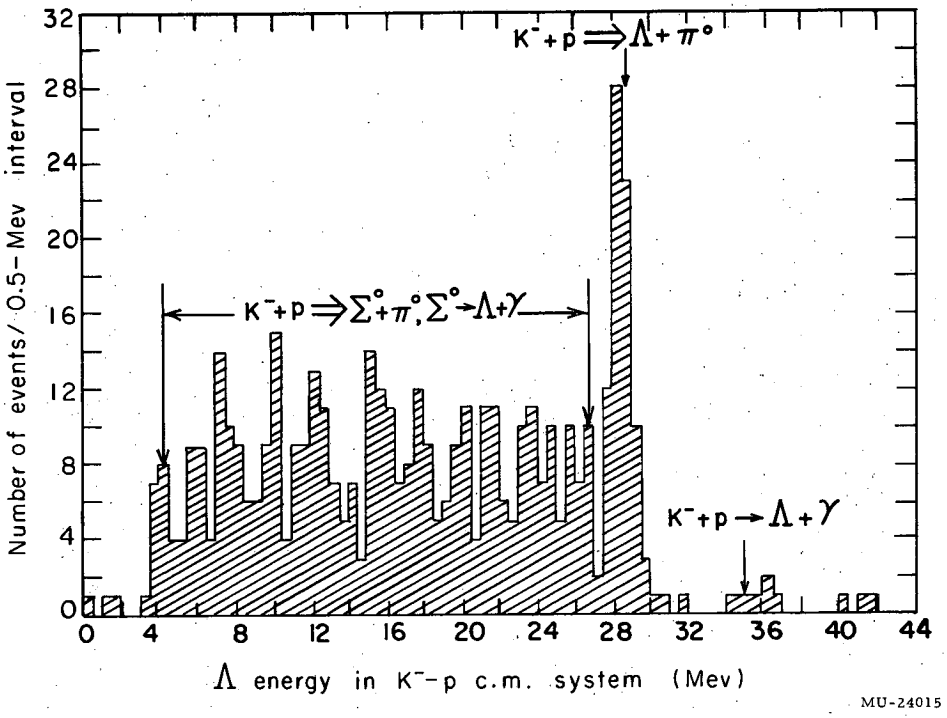

Fig. 13. The observed energy spectrum of Λ hyperons resulting from K^--p interactions at rest. The median of the energy errors is 0.36 Mev.

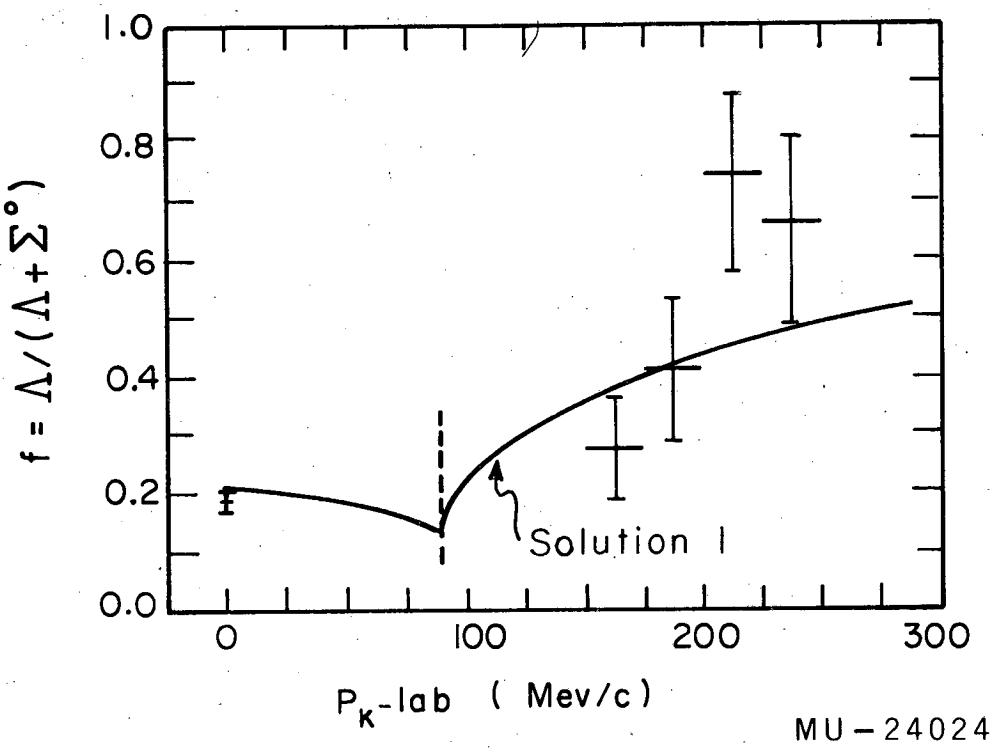

Fig. 14. Branching ratio $\Lambda/(\Lambda + \Sigma^0)$ presented as a function of the K^- lab momentum. The solid curve represents the theoretical prediction for the better of the two scattering length solutions (Solution 1, Table XIII).